JOURNAL OF GEOPHYSICAL RESEARCH, VOL. 102, NO. D20, PAGES 23,895-23,915, OCTOBER 27, 1997

Contribution of different aerosol species to the global aerosol extinction optical thickness: Estimates from model results

Ina Tegen,[1] Peter Hollrig,[2] Mian Chin,[3] Inez Fung,[4,5] Daniel Jacob,[6] and Joyce Penner [7]

Abstract. We combine global distributions of aerosol loading resulting from transport models for soil dust, sulfate, sea salt, and carbonaceous aerosol. From the aerosol distributions we estimate optical thicknesses and compare them with Sun photometer measurements and satellite retrievals, thereby revealing problems with both model results and comparisons with such measurements. Globally, sulfate, dust, and carbonaceous particles appear to contribute equally to the total aerosol optical thickness. Owing to the different optical properties of different aerosol types, aerosol composition should be taken into consideration for estimating the aerosol climate effect as well as for aerosol retrievals from satellite measurements.

1. Introduction

Tropospheric aerosols are a potentially important climate forcing factor [*Intergovernmental Panel on Climate Change,* 1994]. Changes in aerosol loads and distribution should be taken into account for climate change scenarios. Information about aerosol morphology and chemical composition is needed to determine the wavelength dependent backscatter and absorption of incoming solar and outgoing thermal radiation: Knowledge of only extinction optical thickness of the aerosols is not sufficient to assess direct and indirect aerosol forcing [*Lacis and Mishchenko,* 1995]. Aerosol types like tropospheric sulfate that are affecting the radiation budget only by backscattering of solar radiation cause an increase of planetary albedo that leads to atmospheric cooling. On the other hand, absorbing aerosol types like black carbon or soil dust may not change the global radiation budget at the top of atmosphere, but by causing increased atmospheric heating at layers with high aerosol load, they have the potential to change atmospheric circulation.

[1]Department of Applied Physics, Columbia University, and NASA Goddard Institute for Space Studies, New York.
[2]Department of Geography, Division of Climate Research, Swiss Federal Institute of Technology, Zurich, Switzerland.
[3]School of Earth and Atmospheric Sciences, Georgia Institute of Technology, Atlanta.
[4]NASA Goddard Institute for Space Studies, New York.
[5]Also at School of Earth and Ocean Sciences, University of Victoria, British Columbia, Canada.
[6]Division of Engineering and Applied Science, Harvard University, Cambridge, Massachusetts.
[7]Department of Atmospheric, Oceanic, and Space Sciences, University of Michigan, Ann Arbor.

Copyright 1997 by the American Geophysical Union.

Paper number 97JD01864.
0148-0227/97/97JD-01864$09.00

The short atmospheric lifetime and nonuniform sources of aerosol make their distributions highly variable in space and time. Therefore local (ground-based and aircraft) measurements of aerosols alone are not sufficient to describe the global aerosol distribution. On the other hand, with the current satellite instrumentation it is not possible to distinguish the scattering and absorptive properties of aerosol distributions. Also, retrievals of aerosol distributions from reflectance measurements can not unambiguously deduce the necessary information about aerosol optical properties like refractive indices and particle sphericity.

Global transport models that are validated by ground-based measurements can provide a first estimate of global aerosol distributions in space and time. Results from such models have been used to estimate direct [e.g., *Kiehl and Briegleb,* 1993; *Tegen et al.,* 1996] and indirect [e.g., *Boucher and Lohmann,* 1995] radiative effects of specific aerosols. Estimates of aerosol composition based on transport models for all aerosol species have not yet been carried out but could be used as first guess for satellite retrieval algorithms, as the assumption of only a single aerosol type can lead to errors in aerosol optical thickness retrievals.

In this study we attempt an initial guess at global aerosol composition by combining model results from different transport models for soil dust [*Tegen and Fung,* 1995], sea salt, sulfate [*Chin et al.,* 1996], and carbonaceous aerosols [*Liousse et al.,* 1996]. The resulting product shows not only global distributions but also seasonal changes in the composition of the major aerosol types.

2. Description of Transport Models

2.1. Soil Dust

Global dust distributions were calculated with a tracer model as described by *Tegen and Fung* [1995] where dust emission is calculated as depending on soil mois-

ture, surface wind speed, soil texture, and soil surface conditions. The model calculates dust sources, transport, and deposition for eight particle size classes between 0.01 and 10 μm. Global distributions of clay (particles smaller than 1 μm) and small silt (particle radius between 1 and 10 μm) distributions were derived from a global soil texture data set [*Zobler,* 1986; *Webb et al.,* 1991]. The shape of the clay size distribution was fitted to measured dust size distributions near source areas [*d'Almeida and Schütz,* 1983; *Gomes et al.,* 1990; *Patterson and Gillette,* 1977]. Gravitational settling increases quadratically with particle size. Therefore, the shape of silt size distribution aloft is mainly determined by the different settling velocities.

In the model, the amount of uplifted dust follows [*Gillette,* 1978]

$$q_a = C(u - u_{tr})u^2 \tag{1}$$

where q_a is the dust flux from the surface, u is the surface wind speed, and u_{tr} is a threshold velocity. A threshold surface wind speed at 10-m height of 6.5 m s^{-1} was chosen, corresponding to *Kalma et al.* [1988]. The dimensional factor C is taken to be constant for all size classes. European Centre for Medium-Range Weather Forecasts (ECMWF) (Tropical Ocean-Global Atmosphere (TOGA) Analysis) wind products (10-m surface winds) with a spatial resolution of 1.125° × 1.125° and 6-hour time resolution were used as surface wind data. Using this parameterization, the dust fluxes are updated every 6 hours in the transport model.

The seasonal variation of dust uplift is described by the seasonality of surface winds and soil wetness. Dust transport is calculated with the three-dimensional (3-D) Goddard Institute for Space Studies (GISS) tracer model (4° × 5° horizontal resolution, nine vertical layers) [e.g., *Prather et al.,* 1987; *Fung et al.,* 1983]. Dust is removed from the atmosphere by dry and wet deposition. Wet deposition was parameterized by applying high-frequency statistics to monthly mean precipitation data [*Shea,* 1986]. Dry deposition was described by gravitational settling and turbulent mixing as given by *Genthon* [1992]. Atmospheric lifetimes for the different particle sizes range from 230 hours for 0.15-μm particles (washout by rain is the main removal mechanism) to approximately 30 hours for 8-μm particles (gravitational settling is the main removal mechanism). The size distribution only changes due to different settling velocities of different particle sizes; the particles are assumed not to interact with each other and not to grow hygroscopically.

The model calculates dust distribution in space and time as well as particle size distribution. Because of the lack of detailed information on soil surface conditions in potential source areas, the modeled dust source areas will not in each case agree with the actual dust sources but will give a reasonable first estimate. The dust distribution from disturbed soils compared with the distribution from natural soils is described by *Tegen and Fung* [1995]. "Disturbed" dust sources are soils affected by deforestation, cultivation in dry regions, wind erosion, and the shift in the Saharan-Sahelian boundary [*Middelton,* 1992; *World Resources Institute,* 1992; *Tucker et al.,* 1991]. Observed features like the seasonal shift of the Saharan-Sahelian dust plume and the relatively small contribution of dust from Australia can be explained best with a scenario of a 50% contribution of dust from disturbed soils to the total dust load.

2.2. Sea Salt

The global distribution of sea salt aerosol was simulated using a model similar to the soil dust model. Like dust emissions, sea-salt aerosol emissions are highly dependent on surface wind speed. The empirical relationships

$$Q = e^{0.16u+1.45} \qquad (u < 15 \text{ m/s}) \tag{2}$$

and

$$Q = e^{0.13u+1.89} \qquad (u > 15 \text{ m/s}) \tag{3}$$

(where u is the surface wind speed) for the first layer concentration Q of sea salt (in μg/m^3) [*Erickson et al.,* 1986] and

$$r = 0.422u + 2.12 \tag{4}$$

for the sea salt mass median particle radius r (in μm) [*Erickson and Duce,* 1988] in the surface layer were used to describe sea-salt sources and size distributions. Here salt concentrations are directly calculated from surface wind speeds, in contrast to the soil dust model, where emission fluxes were calculated. First layer concentrations and particle radii were calculated using the 6-hourly ECMWF wind products that were also used for calculating dust uplift. Sea-salt size distribution was described for six particle size bins from 2 to 16 μm with limits at 2, 2.5, 3.5, 5, 7, 10, and 16 μm. The resulting size distribution is only an approximation, as only the median size per 6-hour interval can be calculated in this way. There is the possibility that submicron-size sea-salt particles are produced as well, which would lead to an increase of specific extinction efficiency of sea-salt aerosol, but there are few measurements of sea-salt size spectra. Another possible source of errors is that we neglected salt particle size dependence on specific humidity.

Monthly sea-ice data [*Reynolds and Marisco,* 1993] were used to mask areas where ice coverage inhibits sea-salt deflation. Like soil dust, salt transport was calculated using the 3-D GISS tracer model (4° × 5° horizontal resolution, nine vertical layers). Gravitational settling is the main deposition process because of the large particle sizes of sea salt. Settling velocities were calculated using Stokes law with $v_{\text{stk}} = 2\rho r^2/9\nu g$ where ρ is the particle density, g is the gravitational acceleration, and ν is the air viscosity.

Maximum salt concentrations are 57 μg/m^3 in January at 30°W and 50°N, where the mean surface wind speed is 12.7 m/s. In the southern hemisphere (SH), where wind speeds are higher in the annual mean, the maximum sea-salt concentration (43 μg/m^3) occurs in September around 80°E and 50°S, where $u \approx 11.9$ m/s. Additionally, the ECMWF ocean surface wind speed variability is higher in the northern hemisphere (NH)

than the SH, with a maximum u of approximately 30 m/s in the NH compared with 25 m/s in the SH location. This causes a higher maximum sea-salt concentration in the northern hemisphere location at 50°N in the model, even though the annual mean wind speeds are higher at the SH site (10.7 m/s) than at the NH site (9.3 m/s).

Approximately 70% of the modeled aerosol mass is contained in the first four model layers (below approximately 5 km). Figures 1a–1d show a comparison of monthly mean sea-salt concentrations in the first model layer at four locations compared with multiyear surface measurements at Barbados, Miami, Oahu, and Midway of airborne Na and Cl concentrations (measurements from D. Savoie, Rosenstiel School of Marine and Atmospheric Sciences, Miami, Florida). The wind-sectoring of the used aerosol samplers may lead to some bias in the sampling. This could, for example, explain the overestimate of the model results compared with the observations at the Midway station, as here the sampler is located at the east side of the island; as major storm systems move from west to east, the winds would often be out of sector during storms. The measurements were averaged for the years 1982–1994. The Na and Cl

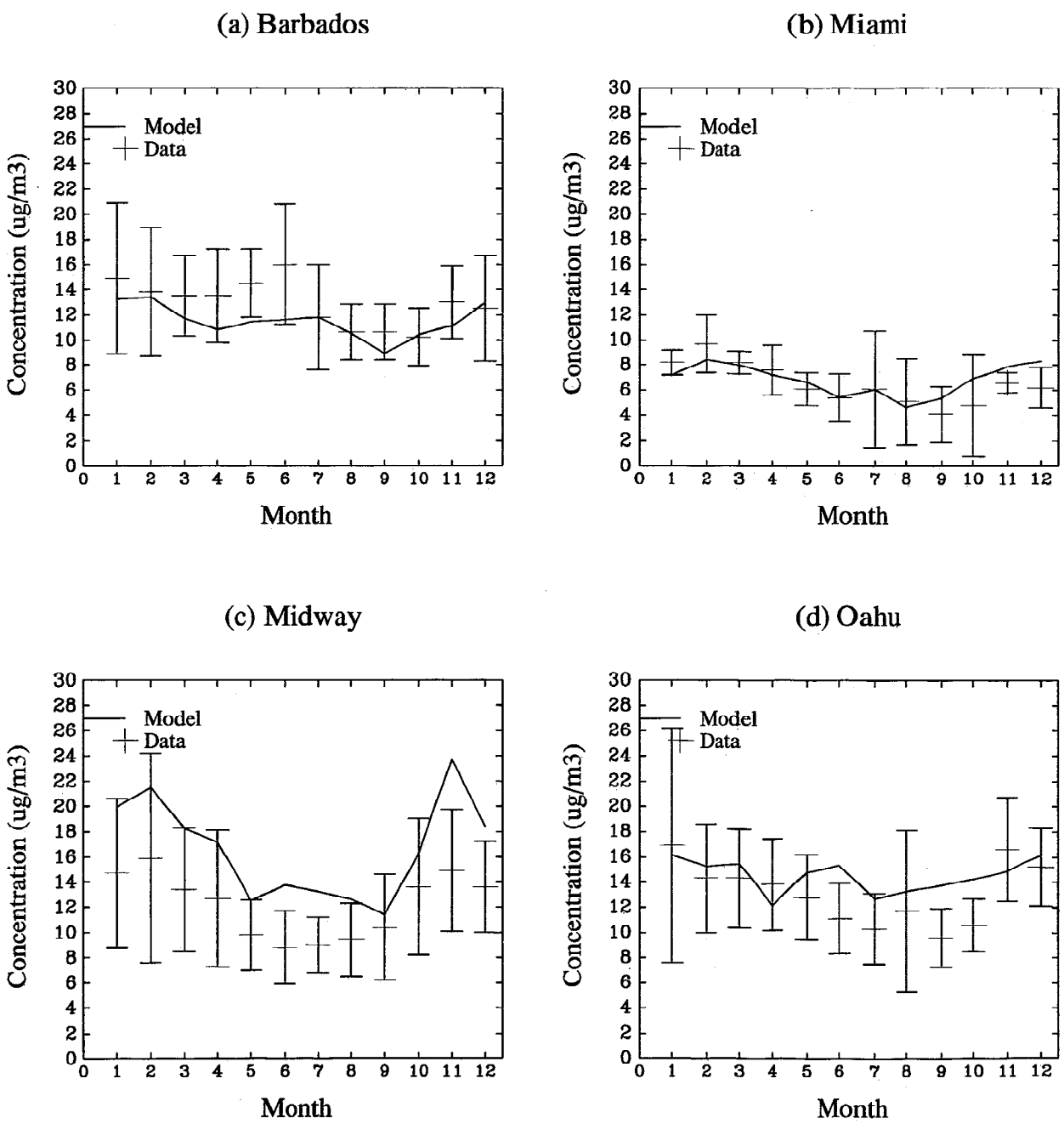

Figure 1. Comparison of sea-salt concentrations from the transport model and measurements at (a) Barbados, (b) Miami, (c) Midway, and (d) Oahu (measurements from D. Savoie, Rosenstiel School of Marine and Atmospheric Sciences, University of Miami).

concentrations give a lower limit for the total airborne sea-salt loads, as these salts also contain other ions like K^+ or SO_4^{2-} so that the "true" sea-salt concentration may be higher. Typically, Na and Cl contribute about 90% to the sea-salt mass [*Oceanography Course Team,* 1989]. A different option would be to use only Na values and average sea-salt composition to calculate sea-salt concentrations, but this is only a minor source of uncertainty.

Because the whole ocean surface area acts as source for sea-salt aerosol all the time, the sea-salt concentrations above the ocean surface are much less variable in space and time than, say, dust aerosol concentrations. Generally, the modeled concentrations lie in the range of the measured concentrations. As the salt particles have short lifetimes, their concentrations are directly related to the surface wind speed, and a good agreement can be expected by using the high-resolution ECMWF surface wind speed product.

2.3. Sulfate Aerosols

The global atmospheric sulfate concentrations have been modeled by several groups [e.g., *Langner and Rodhe,* 1991; *Pham et al.,* 1995; *Chin et al.,* 1996]. In this study we include the 3-D distribution modeled by *Chin et al.* [1996] which also uses the GISS tracer model for atmospheric transport. The model describes the sources, sinks, and transformations of SO_2, Dimethylsulfide (DMS), Methanesulfonate (MSA), and SO_4^{2-}. The model sources of SO_2 were based on the global emissions inventories activity GEIA database [*Benkovitz et al.,* 1996] for the year 1985 with addition of a volcanic and biomass burning SO_2 source. Although industrial emissions in the United States and Europe may have decreased since 1985, the GEIA emission inventory represents a community standard. SO_2 emissions and DMS emission rates were computed as a function of seawater DMS concentrations from *Bates et al.* [1987] and wind speed at 10 m. MSA and SO_2 are produced by DMS oxidation, and SO_4^{2-} is produced by oxidation of SO_2 by OH and H_2O_2. The concentrations of these oxidants were calculated using the photochemical model of *Spivakovsky et al.* [1990]. The results from *Chin et al.* [1996] indicate that fossil fuel combustion is responsible for 68% of the global sulfur emissions, and the global annual source strength of SO_4^{2-} is 49 Mt (S). Wet deposition of SO_4^{2-} was computed using the scavenging scheme of *Balkanski et al.* [1993] which accounts for scavenging in wet convective updrafts as well as for first-order losses in large-scale precipitation. The model used convection and precipitation fields derived from the GISS General Circulation Model (GCM) II. Dry deposition was calculated using the resistance-in-series scheme of *Wesley and Hicks* [1977], where aerodynamic resistance is parameterized as a function of wind speed, solar radiation, cloud cover, and terrain. The model results in an atmospheric lifetime of 3.9 days for sulfate aerosol. *Chin et al.* [1996] presented a detailed evaluation of model results with observations for sulfate and its precursors. The model reproduces typically to within 30% observed sulfate concentrations and wet deposition fluxes measured over the United States and Europe. Sulfate concentrations over the southern hemisphere oceans are reproduced to within 50%. The model underestimates observed sulfate concentrations over the North Pacific and the North Atlantic, partly because of precipitation anomalies in the GCM. Sulfate concentrations simulated in the free troposphere are lower than in previous global models and more consistent with the few observations available.

The effective size of sulfate aerosol depends on the relative humidity and also on the history of the particle, as the humidity dependence of sulfate particles shows an hysteresis effect [e.g., *Kiehl and Rodhe,* 1995]. Additionally, the particle sizes would be different if the particles have been processed through clouds compared with particles that are freshly produced by homogenous nucleation. As this information is unavailable, we cannot assume a realistic size distribution for those sulfate particles.

2.4. Carbonaceous Aerosols

Liousse et al. [1996] simulated carbonaceous (organic and and black carbon) aerosol distributions using a global 3-D transport model, Grantour, which uses wind and precipitation fields of the community climate model (CCM1) [*Walton et al.,* 1988]. Grantour has a horizontal resolution of approximately 4.5° × 7.5° and 12 vertical layers. The authors developed detailed emission inventories for those aerosol species from biomass burning sources (wood fuel, charcoal burning, dung, charcoal production, agricultural fires, savannah, and forest burning) and fossil fuel sources. An estimate for natural sources of organic carbon emissions is also given, excluding natural fires of the temperate and boreal regions. In the case of fossil fuel sources a constant ratio of black carbon to organic carbon emissions was assumed. The authors estimate the global source strength of carbonaceous particles from biomass burning to be 45 Mt/yr (6 Mt/yr black carbon) and 29 Mt/yr from fossil fuel burning (7 Mt/yr black carbon). Natural sources contribute 8 Mt/yr to the atmospheric organic matter. The aerosols from biomass burning sources were injected into the first 2000 m, while the aerosols from fossil fuel sources were injected into the first 1000 m. Dry deposition was calculated with a constant deposition velocity of 0.1 cm/s and wet deposition was calculated by using removal rates of 0.6 cm^{-1} for convective and 2.1 cm^{-1} for stratiform precipitation. Generally there was good agreement between model predictions and observations of surface concentrations and concentrations in precipitation. The results were found to be highly sensitive to the choice of scavenging coefficient and injection height. As for sulfate, the model does not include size information, about which little information is available.

3. Optical Thickness

The wavelength dependent extinction optical thickness of a given aerosol distribution depends on the

mass load, effective radius, and refractive index of the aerosol. For a given mass load m (column mass per surface area) the aerosol optical thickness τ can be calculated with $\tau = 3Q_{\text{ext}}m/4\rho r_{\text{eff}}$, where ρ is the particle density, r_{eff} is the effective particle radius, and Q_{ext} is a wavelength dependent dimensionless extinction efficiency factor [*Lacis and Mishchenko,* 1995]. The (wavelength dependent) value $B = 3Q_{\text{ext}}/4\rho r_{\text{eff}}$ is sometimes called specific extinction cross section. If ρ, r_{eff}, and Q_{ext} are known, the aerosol optical thickness τ can be calculated with $\tau = Bm$ from a mass load m. The disadvantage of estimating aerosol optical thickness from column mass loads and specific extinction is the loss of information about the vertical distribution. Especially for the case of absorbing aerosols, the vertical distribution is crucial for estimating the the climate effect [*Lacis and Mishchenko,* 1995].

For sea salt and soil dust the transport model directly calculates size distributions that are used to estimate optical thicknesses for these aerosol types. In the case of sulfate and carbonaceous aerosols the models do not calculate particle size distributions directly; for those types we use estimates for specific extinction cross sections from the literature.

Table 1 summarizes the ranges for specific extinction cross sections B that were used to estimate extinction optical thicknesses at a reference wavelength of $0.55\,\mu$m from the model-derived aerosol loads. For sea-salt aerosol we chose for B a range of 0.2–$0.4\,\text{m}^2\,\text{g}^{-1}$. The value of $0.4\,\text{m}^2\,\text{g}^{-1}$ is given by *Andreae* [1995], while the value of $0.2\,\text{m}^2\,\text{g}^{-1}$ would be consistent with the modeled sea-salt size distribution under the assumption that no particles with radii smaller than $2\,\mu$m exist. As sea-salt particles with radii as small as $0.03\,\mu$m have been found [*Meszaros and Vissy,* 1974], the value $0.2\,\text{m}^2\,\text{g}^{-1}$ gives a lower limit to the specific extinction of sea-salt aerosol.

The specific extinction for soil dust is described for the size fractions with radii between 1 and $10\,\mu$m (silt fraction) and radii less than $1\,\mu$m (clay fraction). For the silt fraction a mean value of $0.3\,\text{m}^2\,\text{g}^{-1}$ (range 0.2–$0.4\,\text{m}^2\,\text{g}^{-1}$) can be calculated as described by *Tegen and Lacis* [1996]. There are few measurements of the size distribution of submicron clay particles. From size measurements taken close to source areas [*Patterson and Gillette,* 1977; *d'Almeida and Schütz,* 1983; *Gomes et al.,* 1990] we derived a range of 1.2–$1.7\,\text{m}^2\,\text{g}^{-1}$ with a best estimate of $1.5\,\text{m}^2\,\text{g}^{-1}$ for B. To account for the uncertainty of the clay mass contribution, we chose a range of 1–$2\,\text{m}^2\,\text{g}^{-1}$ for the specific extinction cross section of clay size dust.

Specific extinction of dry sulfate aerosol has been assumed to be about $5\,\text{m}^2\,\text{g}^{-1}$ at a wavelength of $0.55\,\mu$m [*Kiehl and Briegleb,* 1993]. Sulfate aerosol is subject to hygroscopic growth, depending on the relative humidity [e.g., *Charlson et al.,* 1984]. *Kiehl and Rodhe* [1995] give a relation for the increase in sulfate extinction cross section to global boundary layer relative humidities. Using these relations, we derive a range of 5–$8.5\,\text{m}^2\,\text{g}^{-1}$ over land and 7–$14\,\text{m}^2\,\text{g}^{-1}$ over ocean areas (based on higher

Table 1. Results from Global Transport Models for the Different Aerosol Types, Assumptions for Specific Extinction Efficiencies B That were Used for Estimating Extinction Optical Thicknesses, and mean Global Mean and Maximum of Calculated Extinction Optical Depths Using These Values.

Type	Source Strength, $\text{Tg}\,\text{yr}^{-1}$	Mean Load $\text{mg}\,\text{m}^{-2}$	B $\text{m}^2\,\text{g}^{-1}$	Optical Thickness (mean)	Optical Thickness (maximum)
Sea salt	5900	22.4	0.2-0.4 (0.3)[a]	0.007	0.02
Soil dust (1-10 μm)	1000	21.6	0.2-0.4 (0.3)	0.007	0.59
Soil dust (<1 μm)	250	14.7	1-2 (1.5)	0.022	0.85
Sulfate (H_2SO_4)[b]	150	3.0	5–12 (8.0)[c]	0.025	0.26
Carbonaceous aerosol[d]	81	2.5	5–12 (8.0)	0.019	0.25
Black carbon	12	0.3	8–12 (9.0)	0.003	0.05

References are sea salt, this study; soil dust, *Tegen and Fung, 1995*; sulfate, *Chin et al., 1996*; and carbonaceous aerosol and black carbon, *Liousse et al., 1996.*

[a] Number in parentheses is used to calculate optical thicknesses given in this table; values are for 0.55-μm wavelength.

[b] Sulfate aerosol assumed to consist of H_2SO_4.

[c] Values are 5–8.5 (6.0) $\text{m}^2\,\text{g}^{-1}$ over land and 7–14 (10) $\text{m}^2\,\text{g}^{-1}$ over oceans.

[d] Carbonaceous aerosol includes black carbon.

average relative humidity over oceans) for sulfate specific extinction cross sections with values of $6\,m^2\,g^{-1}$ over land and $10\,m^2\,g^{-1}$ over oceans as central values. We chose this wide range rather than give a direct humidity dependence for B because the humidity dependence of the sulfate particle size has a hysteresis effect and the particle size is also dependent on whether the particle had been subject to cloud processing. A refined method of estimating B directly from relative humidities would require hitherto unavailable information about the history of the sulfate particle. The assumption for sulfate aerosol particles to consist of ammonium sulfate instead of sulfuric acid [e.g., *Dentener and Crutzen,* 1993] would increase the optical thicknesses calculated from the sulfate loads, but *Kiehl and Briegleb* [1993] argue that this would increase sulfate specific extinction efficiency by only 5%. This may lead to an additional error in the optical thickness calculations, which was neglected here. It should be noted that the value of $B = 10\,m^2\,g^{-1}$ over oceans is likely to be an upper limit for sulfate extinction, as a considerable part of the sulfate could be found above the marine boundary layer where the relative humidity is lower.

For carbonaceous aerosol, *Liousse et al.* [1996] cite references for extinction cross sections with B ranging between 5 and $12\,m^2\,g^{-1}$ for organic and between 8 and $12\,m^2\,g^{-1}$ for black carbon aerosol. We assumed a similar humidity dependence of B for organic aerosol as for sulfate aerosols, although their humidity dependence might be less. For black carbon aerosol, no humidity dependence was assumed, and a value of $9\,m^2\,g^{-1}$ [*Liousse et al.,* 1996] for B was chosen.

4. Scenarios and Results

Table 1 summarizes the assumptions and results for source strengths, mean mass loads, specific extinction, and annual mean and maximum optical thicknesses for the different modeled aerosol types (sulfates, soil dust, organic aerosols, black carbon, and sea salt). For this study we did not distinguish between aerosols with natural or anthropogenic sources. To determine the mass of the sulfate aerosol, it was assumed to be composed of pure sulfuric acid. The coarse mode aerosols (sea salt and soil dust) have the highest mass loads but are not dominating the total optical thickness due to their small specific extinction cross sections. Nevertheless, the contribution of soil dust to the global extinction optical thickness is comparable to the extinction attributable to sulfate and carbonaceous aerosol [*Li et al.,* 1996]. In the global mean, those three aerosol types contribute equally to the global mean aerosol extinction optical thickness. Dust particles smaller than $1\,\mu m$ (clay particles) have a significantly higher global mean mass load than sulfate aerosol, although their source strength is of comparable magnitude. This is probably caused by the more efficient wet scavenging of sulfate aerosol (in-cloud removal (washout) and sub-cloud scavenging (rainout)) compared to dust aerosol (rainout only). Also, dust aerosol is produced in arid and semiarid areas with low precipitation rates, while on the other hand, about 85% of the sulfate aerosol originates from in-cloud oxidation in areas with higher precipitation rates. Therefore wet deposition is a more effective removal mechanism for sulfate than for soil dust. By comparing the maxima with the annual and global means of the modeled optical thicknesses, we find that sea-salt production is relatively constant over space and time, while the high ratio of maximum to mean optical thickness of the soil dust aerosols illustrates the high spatial and temporal variability of this aerosol type.

The total model-derived extinction optical thickness (at a reference wavelength of $0.55\,\mu m$) for the four seasons is given in Plates 1a–1d. Features like the seasonal shift of the Sahelian-Saharan aerosol plume (caused by dust and carbonaceous aerosols) and the high aerosol load over China in the northern hemisphere spring and over Saudi Arabia in summer (caused by dust) are reproduced by the modeled optical thickness distribution. The dust plume over the North Atlantic originating from the Saharan-Sahelian region may be underestimated due to underestimating peak winds; because of the high unlinearity of wind speed dependence of dust deflation, large errors may be the consequence of insufficient resolution of the ECMWF surface wind speed products. Also, the long-range transport of dust is underestimated for cases of heavy dust load, a problem common with all dust models. In the southern hemisphere the optical thicknesses appear to be rather high for the South Pacific around Australia, which may be caused by the dust model overestimating Australian dust production. The biomass burning plume from South America over the South Atlantic is not visible in the advanced very high resolution radiometer (AVHRR) retrievals, which may be a problem of the retrieval method.

4.1. In-Situ Observations of Aerosol Optical Thickness

Extinction aerosol optical thickness can be obtained from ground-based multichannel Sun photometer measurements. The Goddard Space Flight Center [*Holben et al.,* 1996] provides an on-line database of a worldwide network of Sun photometer sites where since 1992 aerosol optical thicknesses are measured at different wavelengths over different timescales. The instruments used for these optical thickness retrievals are Sun-sky scanning spectral radiometers. They measure the spectral atmospheric extinction of direct beam radiation from which the aerosol optical thickness can be derived according to Beer's law. In this work, optical thickness measurements extrapolated at the reference wavelength of 500 nm measured at a 15-min time interval were averaged over a month and compared with the modeled optical thickness values described previously. We recognize that it is problematic to compare single point measurements with model values that cover an area of approximately $400\times\ 500\ km^2$ and represent a climatological monthly average. The model results are based on averaged emission rates and averaged meteorology and

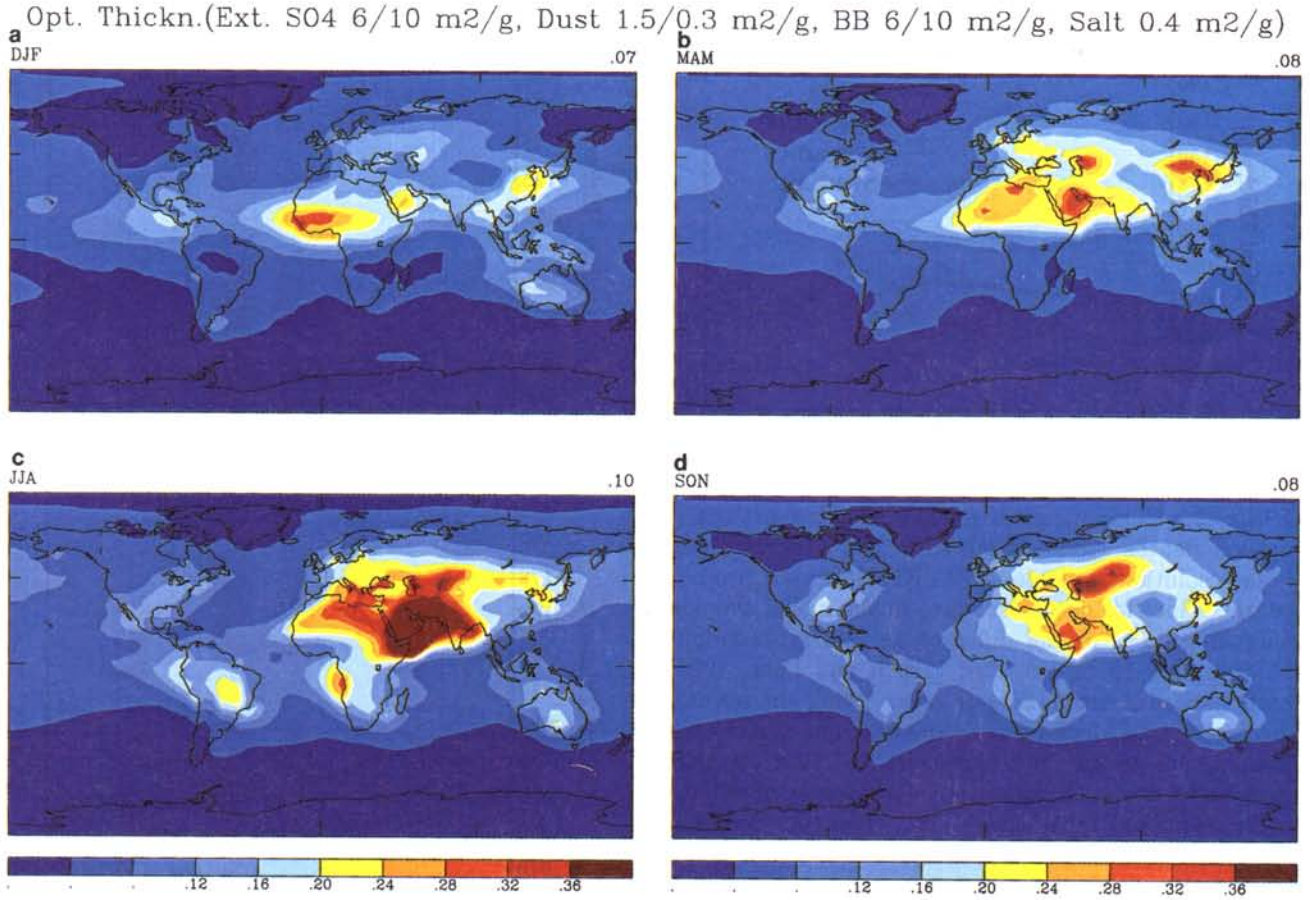

Plate 1. Seasonal variation of combined aerosol extinction optical thickness estimated from transport model results using the values given in Table 1.

often cannot reproduce subgrid-scale spatial variability. For example, monthly mean observations from four different U.S. sites (Jug Bay (38.45°N, 76.46°W, observations from November 1994 to March 1995); SERC (38.53°N, 76.3°W, observations from November 1994 to March 1995); Burtonsville (39.06°N, 76.56°W, observations from December 1994 to March 1995) (these stations are located in the the Chesapeake Bay area about 50 km south of Baltimore and Washington D.C.); and Gaithersburg (39.08°N/77.12°W (located a few kilometer north of Washington, D.C.) observations from December 1994 to March 1995)), which are located in the same model-grid box area vary by a factor of 4 for the same time period. Nevertheless, owing to the lack of satellite retrievals over land, the only way to validate the model aerosol optical thickness (AOT) over land is by comparison with such Sun photometer observations. Figure 2a shows a comparison of the aerosol optical thicknesses measured at those U.S. sites and model results. Analysis of the individual aerosol contribution to the total optical thickness has shown that the sulfate aerosol contributes more than 50% to the total extinction optical thickness, followed by smoke and dust aerosol. Although the model tends to underestimate the observation at some sites, it reproduces the magnitude of the observation quite well. Owing to the lack of sufficient Sun photometer observations in summer, we would be unable to tell whether the model reproduces the seasonal cycle as well. However, ground-based measurements of sulfate concentrations in the eastern United States as referenced by *Chin et al.* [1996] show the same seasonal summer maximum as the model, which is caused by higher oxidation rates of sulfur dioxide because of higher abundance of OH in the summer months. Figures 2b-2f show optical thickness measurements for four stations that are located in regions where biomass burning and dust deflation contribute to high aerosol optical thicknesses.

4.1.1. Soil dust site. Sun photometer sites where the atmospheric dust load is only influenced by soil dust aerosols are hard to find, as those sites are located at desert fringes rather than in deserts themselves. The site Sede-Boker (30.3°N, 34.2°E, observations from April 1995 to August 1996) shown in Figure 2b is located in a region that is dominated by soil dust aerosols, although probably also impacted by European industrial aerosol. The observations were compared with three different model scenarios (minimum,

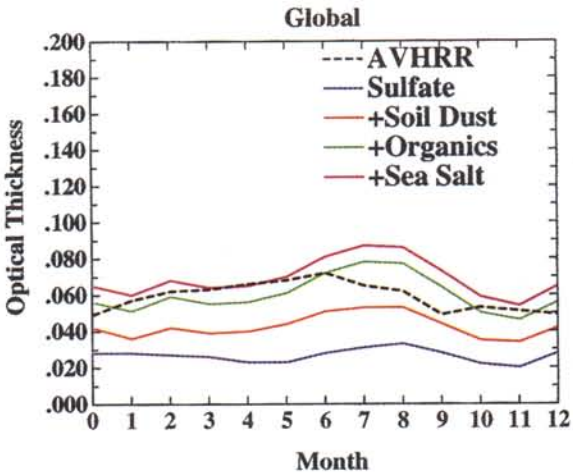

Plate 2. Comparison of model-estimated extinction optical depths (solid lines) with the advanced very high resolution radiometer (AVHRR) aerosol product (dashed line) for ocean locations in the global average. Contribution is of the different aerosol types sulfate [*Chin et al.,* 1996], soil dust [*Tegen and Fung,* 1995], carbonaceous aerosol [*Liousse et al.,* 1996], and sea salt. Aerosol optical thicknesses of the different model components are added up progressively, so that the solid lines show the extinction optical thickness of sulfate, sulfate and soil dust, and so on. The top (red) line shows the combination of all four aerosol types.

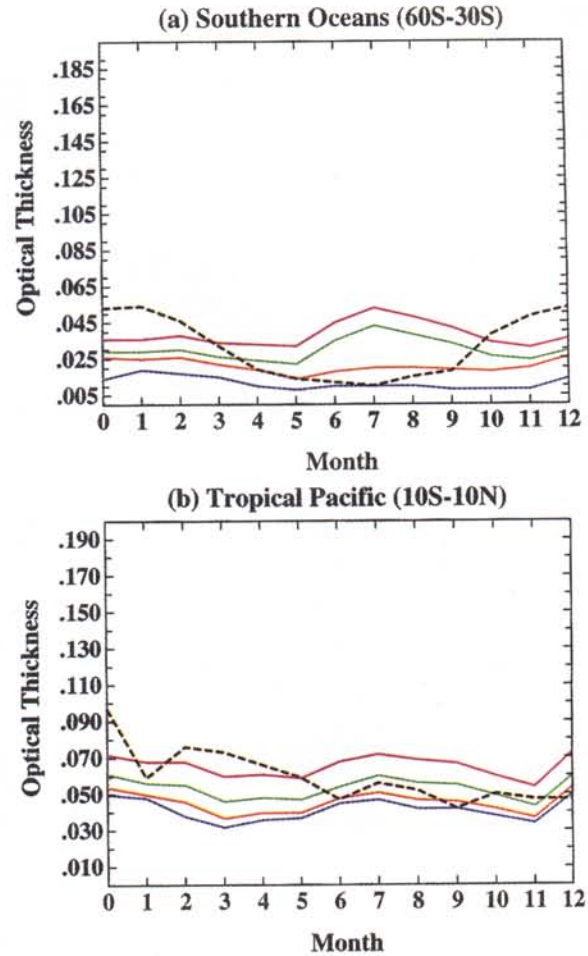

Plate 3. Same as Plate 2 for remote ocean regions.

maximum, and best estimate specific extinction cross section). Although the observed AOT varies for both years with a maximum difference in March by a factor of 4, model and observations show an agreement in magnitude and seasonal cycle. Remarkable also is that the two peak values in April and September simulated by the model were confirmed by the observed AOTs, indicating that the dust transport into this region is reasonably well simulated by the model.

Ouagadougou (Figure 2c) is a town located in Burkina Faso, north of the states of the Ivory Coast. This site is influenced by both soil dust and biomass burning aerosol. Satellite-derived fire distributions [*Cooke et al.,* 1996] indicate that Ouagadougou is not directly situated in a very active fire region but is close to it. Monthly average numbers of fire pixels detected from November 1984 to October 1989 show peak values in November and December in that region. Ouagadougou has a characteristic seasonal pattern of the aerosol optical thickness for this region, with high values during the dry season (Figure 2c). The maximum observed AOT occurs in April, while the model predicts highest values in February. The model generally underestimates the measured aerosol optical thickness during the nonburning season in the NH summer. This is probably caused by the dust model underestimate of the summer soil dust load, which is also obvious in the comparison with the AVHRR optical thickness product (see below).

4.1.2. Biomass burning site. Figure 2d shows the site Mongu (15.3°S, 23.0°E, observation from June to November 1996), located in a region where carbonaceous aerosols are predominant at the time of measurements (burning season is August to September). This comparison shows an agreement of modeled and observed seasonality. However, the magnitude of the AOT during the burning season is underestimated by a factor 2 by the model, indicating that either the estimates of aerosol source strength are too low for this region or the site is strongly exposed to burning events resulting in unusual high AOTs for this period of time compared with area and multiyear averaged model values.

In Figures 2e and 2f two sites (Alta Floresta (9.55°S, 56°W, observations from June 1993 to September 1994) and Cuiaba (15.3°S, 56°W, observations from June 1993 to July 1995)), located in the Amazon basin are shown. Climatologically, this area is divided into a dry (burning) season and a wet (nonburning) season, whereas their durations can vary for different seasons and are mostly dependent on intraseasonal and interannual fluctuations of the meteorological conditions. Recently, *Holben et al.* [1996] refined this relatively simple seasonal pattern by dividing the dry season into four dif-

ferent phases, partitioned after an assumed threshold AOT: preburning season (AOT (440 μm) < 0.4); transition to burning season (AOT (440 μm) = 0.4-1.0); burning season (AOT (440 μm) > 1.0); transition to wet season (AOT (440 μm) = 0.4-1.0); and wet season (AOT (440 μm) < 0.4). The site in Alta Floresta is located in a seasonal forest area where since 1974 forests were extensively burned. The burning season in this region starts in March and extends until late September, whereas most of the biomass burning occurs in August and September [*Artaxo et al.*, 1994]. The site at Alta Floresta shows an agreement between model and observation in the seasonal cycle of AOT. The magnitude of observed AOT occurring in August

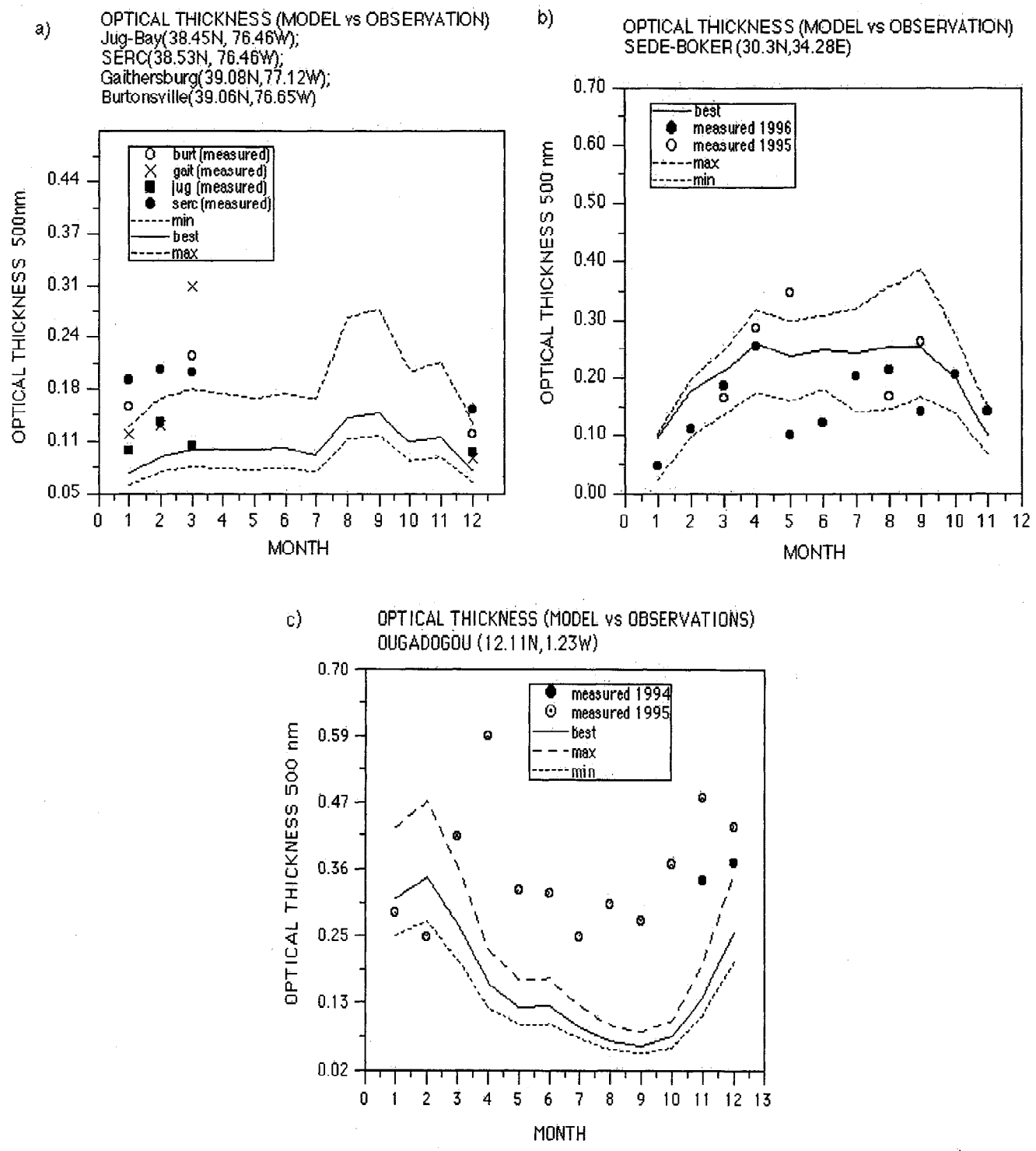

Figure 2. Comparison of seasonal variation of model-estimated extinction optical thicknesses with optical thickness measurements from the Goddard Space Flight Center Sun photometer network for sites (a) Jug Bay, SERC, Burtonsville, and Gaithersburg; (b) Sede-Boker; (c) Ouagadougou; (d) Mongu; (e) Alta-Floresta; (f) Cuiaba; and (g) Hawaii.

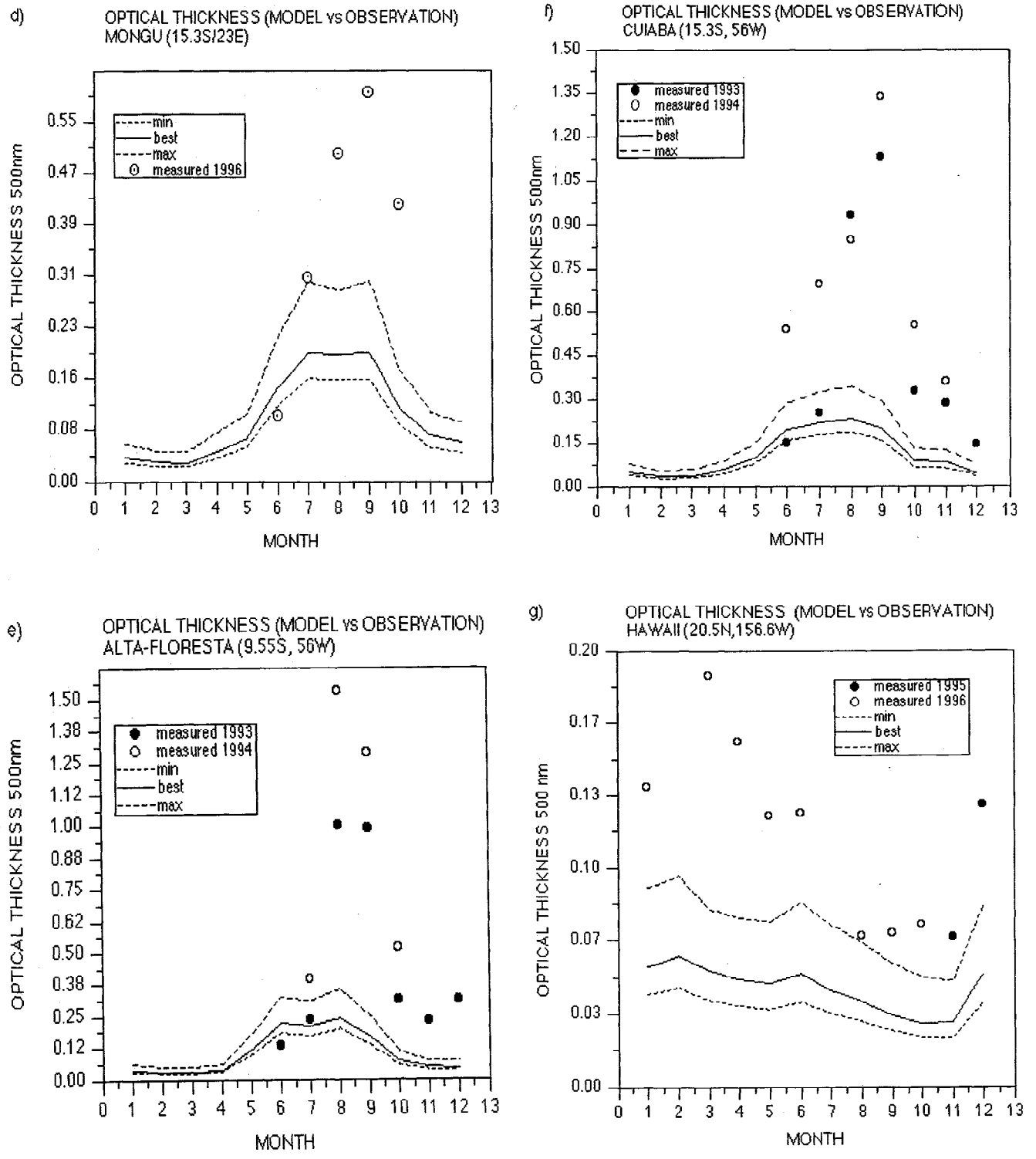

Figure 2. (continued)

and September is underestimated by a factor of 4 by the model. Cuiaba, which is located in the Cerrado region, is exposed to aerosols from anthropogenically induced fires as well as aerosols transported from forest burning regions in the northern part of the Amazon basin. Although the model tends to reproduce the seasonal cycle of the measured AOTs, it does not simulate the peak values in the burning season (August, September). Observations are up to a factor of 5 higher than the model estimates. Measurements of black carbon surface concentration [*Artaxo et al.*, 1994] show that at this particular site the surface concentrations can be up to a factor of 6 higher than the black carbon surface concentration estimated by the model. Higher black carbon surface

concentration also implies higher smoke concentration, which would cause considerably higher optical depths than estimated by the model.

A comparison of modeled biomass burning AOT and AVHRR optical thickness retrievals off South America (see below) show that the AVHRR signal is much lower than the model in this area, which is an indication that the model does not underestimate the biomass burning source in that region. Comparing single-point measurements with area-averaged grid box model values is especially problematic in biomass burning regions, if a Sun photometer is placed in the approximate vicinity of a highly active fire region. In this case, it would measure too high aerosol optical depths compared with an area-average grid box value. In this case, we could estimate from the ratio between modeled and observed optical thickness the percentage of the area that is covered by biomass smoke. For the months August and September, when the burning activity is maximum, this would result in for the Mongu site, 40–50%, for Alta Floresta, 15–25%, and for Cuiaba, 13–22%, of the model grid box area being actually covered by biomass burning aerosol in August and September. A definite answer to this question could only be given by a network of Sun photometers in an area represented by a model grid box.

4.1.3. Remote site. Figure 2g shows a remote site in Hawaii (20.5°N, 156.59°W) where aerosols either originate from local sources (DMS, sea salt, or volcanos) or are transported from biomass burning regions (January–March) or dust aerosol regions (April–June) into this area. The comparison shows a good agreement between model and observation in the seasonal cycle of the AOT. The magnitude is underestimated by the model by a factor of 2 up to a factor of 4 in February and March 1996. Possible reasons for this underestimate can lie either in an underestimation of the local sources or in an underestimation of the long-range transport of dust or biomass burning aerosols into this region. Additional error sources of optical thickness retrievals from Sun photometers can originate from the cloud-screening, in the atmospheric correction of the measured data, and in the calibration and maintenance procedures of the instruments. The cloud-screening procedure contributes probably the biggest uncertainty to the retrieved AOTs.

Uncertainties in model optical thicknesses are caused by uncertainties in parameterizations of sources, transformation processes, and sinks, as well as of the specific extinction cross section. Table 2 summarizes the sensitivity of the dust model to variations in the source strength (between 800 and 1600 Mt/yr for dust particles <10 μm), wet deposition parameterization (upper limit, using a scavenging ratio of 400 for minimum washout, and lower limit, maximum washout by using the the assumption that dust is removed from the whole grid box for a rain event [*Tegen and Fung,* 1994]). The uncertainties in the extinction cross section B (as described above) and the source strength cause an uncertainty in the dust contribution of modeled aerosol optical thickness of factor 2 at all sites. At the remote site (Mauna Loa) the extremal assumptions for the wet deposition parameterization cause also an uncertainty of factor 2, while at a site close to a source region (Sede-Boker) the optical thickness uncertainty caused by the wet deposition parameterization leads only to a 20% variation in the result. For sulfate aerosol, the uncertainties in the model parameterization also lead to an uncertainty in the results by a factor of 2. Results from *Chin et al.* [1996] show that the wet scavenging efficiency of sulfate in convective rain events is very high. As in the case of the dust model, precipitation is not directly coupled with convective mixing, and this may lead to an underestimate of wet deposition of dust.

4.2. Comparison with AVHRR Aerosol Optical Thickness Product

Satellite retrievals of aerosol extinction optical thicknesses have been attempted over oceans under clear sky conditions using data from the from the advanced very high resolution radiometer (AVHRR) instrument [*Rao et al.,* 1988]. The range and pattern of the modeled aerosol distributions show some agreement with the AVHRR retrievals for the period from June 1989 to June 1991. However, assumptions like spherical particle shape or constant ocean albedo in the retrieval algorithm could cause errors in the satellite optical thickness product. Nonspherical particle effects [*Mishchenko and Travis,* 1994] could specifically be a problem in the satellite retrieval of desert dust aerosol, which is associated with the highest observed optical thicknesses over the North Atlantic and the Arabian Sea. We use the AVHRR product for qualitative comparison with model-derived aerosol spatial and temporal distributions but not necessarily for validation of the magnitude of total extinction optical thicknesses. We expect the AVHRR product to underestimate extinction optical thicknesses, as they were retrieved under the assumption of aerosols with single scattering albedo of 1. Also, in cases where aerosols plumes are located below or within clouds, the aerosol signal would be underestimated by the satellite retrievals that give only information for clear-sky conditions if the occurrence of aerosols was correlated with the occurrence of clouds. The AVHRR retrieved optical thickness values can therefore be expected to be generally a lower limit for the extinction optical thickness of aerosols.

Plates 2–6 show the contribution of the different aerosol types from model results (solid colored lines) to aerosol optical thickness in comparison with the AVHRR optical thickness product (dashed black lines) for different ocean locations that are likely to be influenced by different aerosol types. This comparison is divided for regions with different dominant aerosol species, like remote regions, regions with dominant industrial aerosol, soil dust, and biomass burning aerosol.

4.2.1. Global average. In the global mean, the model results indicate that sulfate aerosols contribute about 40–50% to the aerosol optical thickness over the oceans (Plate 2) but only about 30% when averaged over both land and sea (Table 1). A reason for this dif-

Table 2. Sensitivity of Soil Dust Contribution of Model Optical Thickness τ to Uncertainties in Model Assumptions at Three Sun Photometer Sites

	τ	τ	τ	Dust contribution
Dust Source, Mt yr^{-1}	800–1600	800	800	
Scavenging ratio	750	400–750[a]	750	
B, m^2/g^{-1} (clay/silt)	0.3/1.5	0.3/1.5	0.2-0.4/1-2	
Sede–Boquer	0.12–0.23	0.16–0.20	0.12–0.23	70%
Mongu	0.011–0.021	0.013–0.019	0.011–0.021	17%
Mauna Loa	0.010–0.020	0.010–0.022	0.010–0.020	24%

[a] Maximum dust rain-out with the assumption that the rainfall is distributed over the whole model grid box for a rain event

ference is that sulfate aerosol is mainly produced by oxidation of SO_2 (this process takes place over the oceans as well as over land) and has also oceanic sources, while dust and carbonaceous aerosols are emitted as particles from continental sources and are removed from the atmosphere relatively close to their source areas due to their short atmospheric lifetime. The contribution of sea-salt particles to the global aerosol extinction is small. As submicron-size sea-salt particles may not be adequately modeled by equation (4), the contribution of this aerosol type may be underestimated.

4.2.2. Remote regions. At remote ocean regions (Plates 3a and 3b), sea-salt aerosol contributes up to 30% to the total aerosol optical thickness. Although the magnitude of the aerosol signal in the Southern Oceans (Plate 3a) agrees for model and observations, the seasonal signal is reversed. This may be because the modeled biomass burning signal from South America is not detected by AVHRR (see also Plates Figures 6b and 6c). In the tropical central Pacific (Plate 3b) the AVHRR retrievals are of the same magnitude as the modeled aerosol signal (dominated by sulfate produced by homogeneous and in-cloud oxidation). However, the seasonality of the satellite retrieval is not reproduced by the model, and it is unclear whether this is caused by model deficiencies or retrieval uncertainties.

4.2.3. Regions influenced by industrial aerosols. Over the North Atlantic, those regions that are influenced by aerosols from industrial regions in the eastern United States and Europe (Plates 4a–4c) show a strong summer maximum in the AVHRR aerosol retrieval that is not reproduced by the models. As the seasonal pattern in these regions is dominated by sulfate aerosol, a possible explanation could be the underestimation of the seasonal cycle by the sulfate model from overestimating washout rates downwind off continents [*Chin et al.,* 1996]. In other regions, like the Bay of Bengal (Plate 4d), the South China Sea (Plate 4e), and the north east Pacific (Plate 4f), where sulfate and carbonaceous aerosols from fossil fuel burning are major components, both the magnitude and the seasonality of the aerosol signal are well reproduced. Over the NE Pacific the observed spring maximum could be caused by soil dust transported from Asia (same seasonality but weaker signal than Plate 5d) [*Gao et al.,* 1992]. Over Central America (Plate 4g), insufficient dust transport in the model could explain the lack of a summer maximum in the model.

4.2.4. Dust regions. In the subtropical North Atlantic (Plates 5a and 5b) the aerosol models seem to underestimate the extinction optical thickness if compared with other sites. In that region, soil dust contributes a major part to the aerosol load (with considerable contribution of biomass burning aerosol in the tropical Atlantic (Plate 5b)). Comparisons with long-term mineral dust measurements at Barbados [*Prospero and Nees,* 1986] show that the dust model [*Tegen and Fung,* 1995] underestimates the seasonal shift of the dust plume emerging from Africa from Saharan-Sahelian sources and underestimates dust transport from North Africa during northern hemisphere summer, which would explain this discrepancy. The highest optical thicknesses are found during northern hemisphere summer over the Arabian Sea (Plate 5c). This signal is caused by soil dust from the Near East and East Africa that is transported in association with the summer monsoon. This signal is also well observed in ground-based measurements [e.g., *Ackerman and Cox,* 1989]. In this case the AVHRR retrieval would underestimate the aerosol optical thickness by assuming a nonabsorbing aerosol type, as dust is partly absorbing at solar wavelengths, and also, the assumption of spherical particles would introduce errors in the retrieval of soil dust optical thicknesses. Over the NW Pacific (Plate 5d) the spring maximum aerosol optical thickness is caused by soil dust from China (this signal can be found in the satellite retrievals as well as in the model results). The same problem as over the Arabian Sea (underestimating the soil dust extinction by assuming a totally reflecting aerosol) would occur at locations with high contribution of soil dust aerosol like the Mediterranean and the Black and Caspian Seas (Plates 5e and 5f). On the other hand, in that regions the dust model might also overestimate the dust load.

4.2.5. Biomass burning regions. The seasonal signal in extinction optical thickness over the South Atlantic off the coast of South Africa (Plate 6a) may be caused by biomass burning, although the model predicts the maximum concentrations in July-August [*Liousse et al.,* 1996] while the maximum in the AVHRR

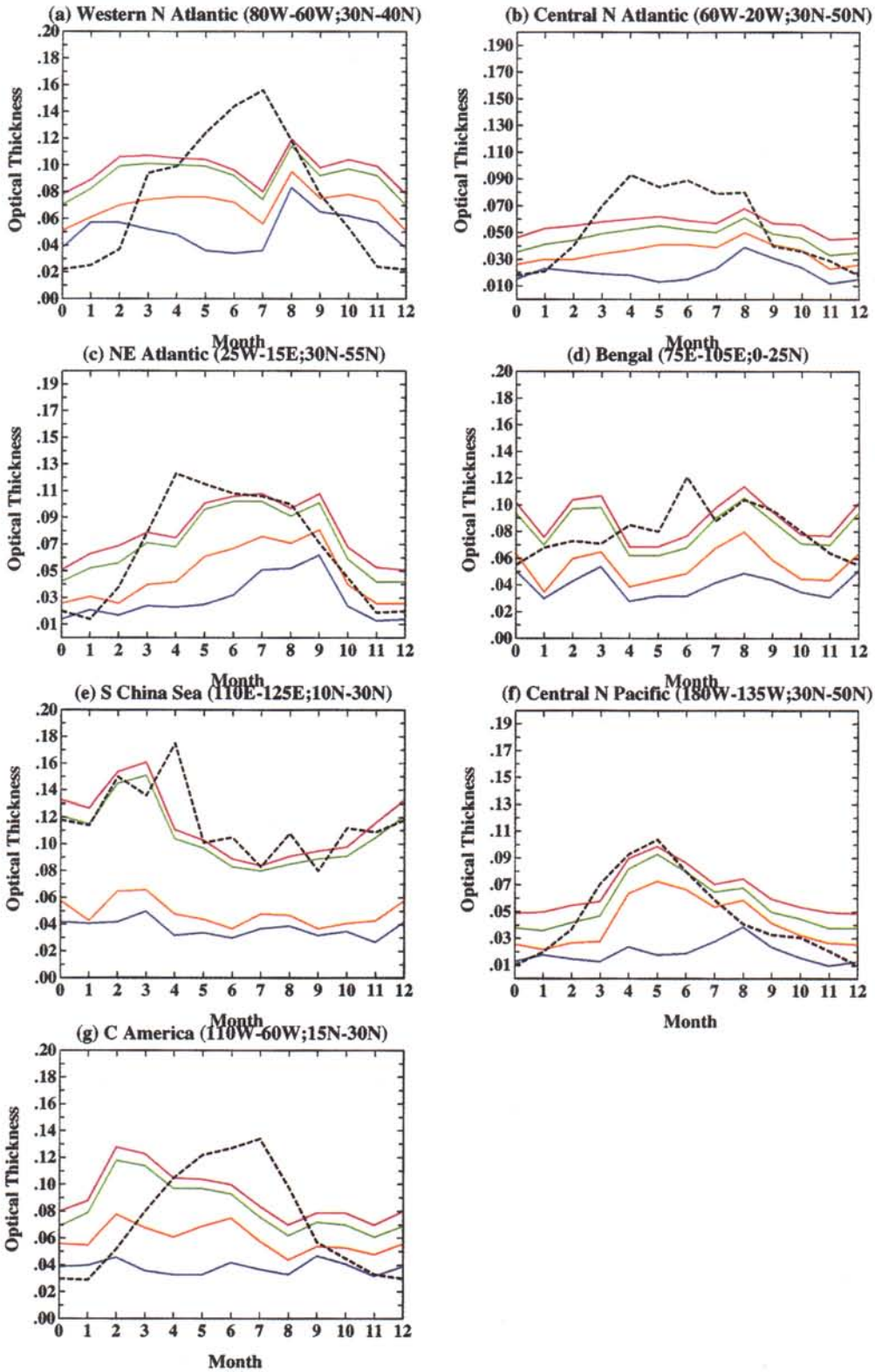

Plate 4. Same as Plate 2 for ocean regions that are primarily influenced by industrial aerosol.

signal is in September. Here the order of magnitude is well reproduced by the model results. On the other hand, large discrepancies between the modeled seasonal cycle of aerosols and the observed AVHRR signals are found at locations that are influenced by biomass burning aerosol from South America (Plates 6b and 6c) in the South Atlantic and South Pacific. There, a strong seasonal cycle caused by biomass burning with a maximum from June to September is observed in ground-based measurements [e.g., *Artaxo et al.,* 1994] and re-

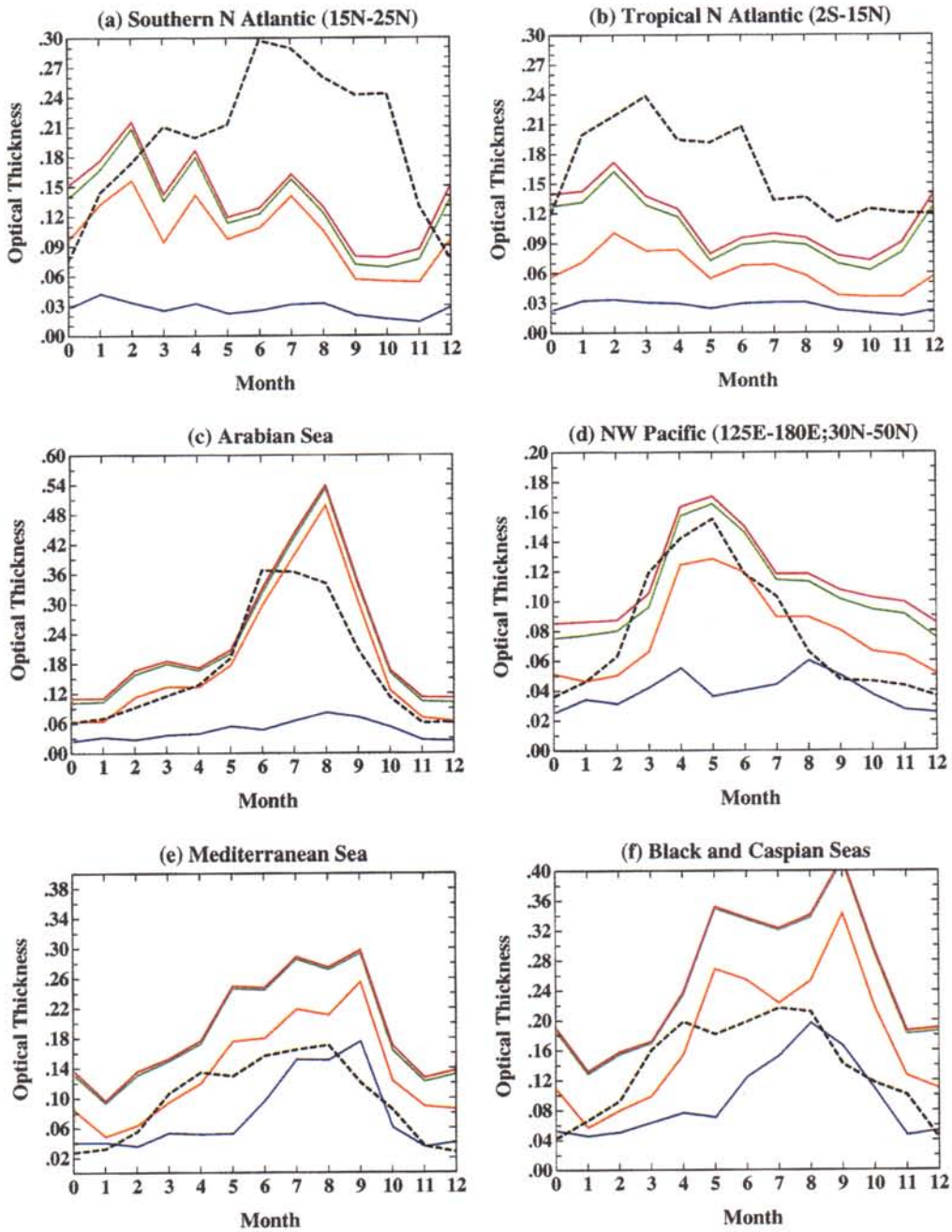

Plate 5. Same as Plate 2 for ocean regions that are primarily influenced by soil dust aerosol.

produced by the model [*Liousse et al.*, 1996], but is not observed by the AVHRR instrument. The lack of an aerosol signal in the satellite retrievals for this region could be explained if the aerosol plumes from burning were often accompanied by cloud coverage that would prevent their detection by AVHRR. In the total ozone mapping spectrometer (TOMS) satellite retrievals of absorbing aerosols, such burning events can be observed but are not very common, which may be related to the fact that the TOMS retrieval is not sensitive to aerosols below 1.5 km; also, if the aerosol plume is completely obscured by clouds it cannot be detected by TOMS either. Indonesia (Plate 8d) is influenced by industrial aerosol as well as by biomass burning in SH spring. The magnitudes of modeled and AVHRR derived optical thicknesses agree well in this location.

4.2.6. Different model scenarios. In Plates 7a–7c we explore the sensitivity of aerosol optical thicknesses to different model assumptions in an attempt to reduce discrepancies between model and satellite analysis. Case A is the "best estimate" case described above. Case B is a case where the biomass burning signal is reduced by a factor of 2, as the specific extinction efficiency for this aerosol type is highly uncertain (as is the carbonaceous aerosol load itself). Case C uses the sulfate aerosol distribution of *Chuang et al.* [1997] instead of *Chin et al.* [1996] where natural and anthropogenic sulfate distributions where calculated with with

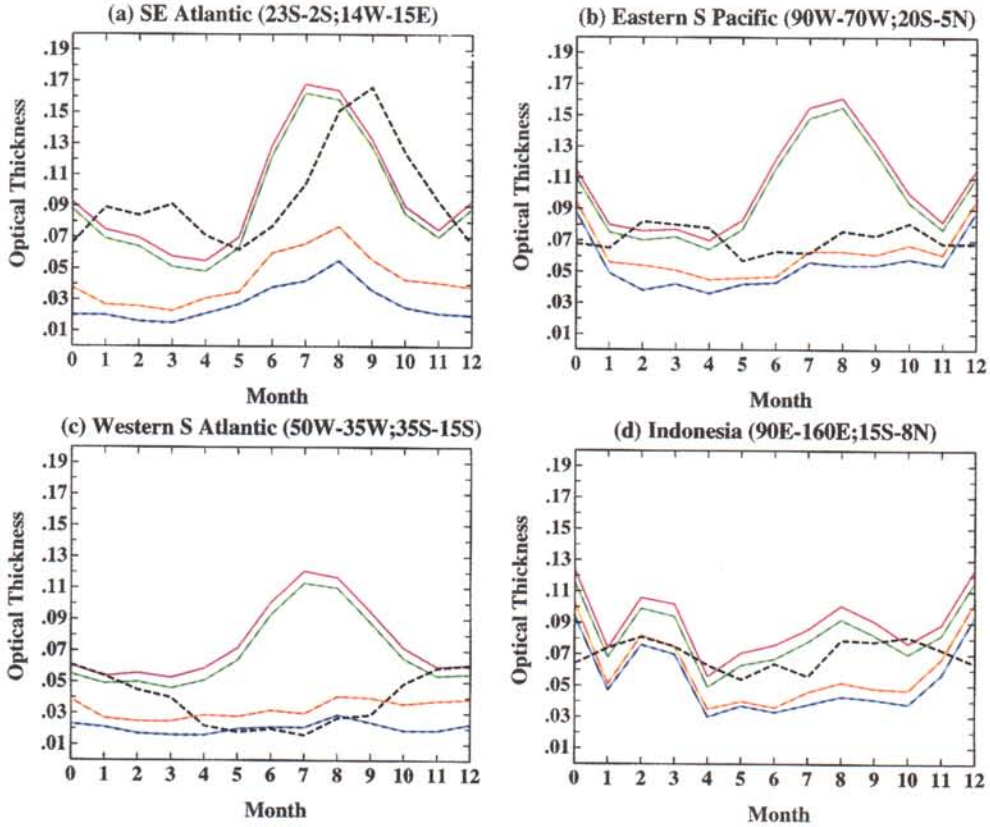

Plate 6. Same as Plate 2 for ocean regions that are primarily influenced by biomass burning aerosol.

the Grantour model. On the basis of this sulfate distribution, direct and indirect sulfate aerosol forcing has recently been estimated [*Chuang et al.*, 1997]. Case D describes the result for the minimum assumption for specific extinction efficiencies B for all aerosol types (Table 1), and case E uses minimum extinction cross sections for absorbing aerosols (dust) and maximum values for the other aerosol types. The results are given for the global average ocean values (Plate 7a) and for the Arabian Sea (highest dust contribution) (Plate 7b, see also Plate 5c) and NW Atlantic (Plate 7c, see also Plate 4a). In the global mean the different model assumptions result in differences of ±30% compared with an average value. If we assume that AVHRR gives a lower limit for ocean AOTs, case D (and, to a lesser extent, case B) can be ruled out. On a global scale, the use of a different sulfate model (case C) does not cause a significant difference to the best guess case (A). Case E seems to overestimate the AOT compared with the AVHRR retrievals but cannot be ruled out due to the retrieval problems.

In the case of the Arabian Sea (Plate 7b), the assumption of a lower dust extinction efficiency leads to a better agreement with AVHRR, but again, in this case we know that AVHRR underestimates the AOT due to the assumption of a dust single scattering albedo of 1 in the satellite retrieval algorithm. Which of the other model assumptions leads to the most realistic AOTs cannot be decided for this case.

For the example of the NW Atlantic (Plate 7c), where a strong influence of anthropogenic sulfate aerosol is expected, the discrepancies between model and observed seasonal cycles are much improved by using the sulfate results from *Chuang et al.* [1997] (case C), which show a summer maximum that agrees better with observations than the seasonality of *Chin et al.* [1996], where the offshore washout of sulfate may be overestimated. The remaining discrepancies in this case could be explained by an overestimate of the winter dust load, or on the other hand, a masking of the aerosol signal in AVHRR by cloud cover in the winter months.

In summary, neither the combination of the results of different aerosol transport models nor the satellite optical thickness product alone are sufficient to explain the aerosol distributions over the oceans, but if combined with ground-based observations, a comparison of both data sets can indicate areas where either the transport models have deficiencies or satellite retrievals may be problematic. Specifically, the aerosol product from the transport models can indicate areas and seasons where the assumption of constant aerosol properties (particle sphericity and single scattering albedos) may cause errors in satellite retrievals.

4.3. Contribution of Absorbing Aerosols

Assumptions of single scattering albedos of 1 for all aerosol types can lead to errors in satellite retrievals of aerosol optical thicknesses. Depending on their origin, aerosols can have typical single scattering albedos of 0.8–1 [*Intergovernmental Panel on Climate Change,*

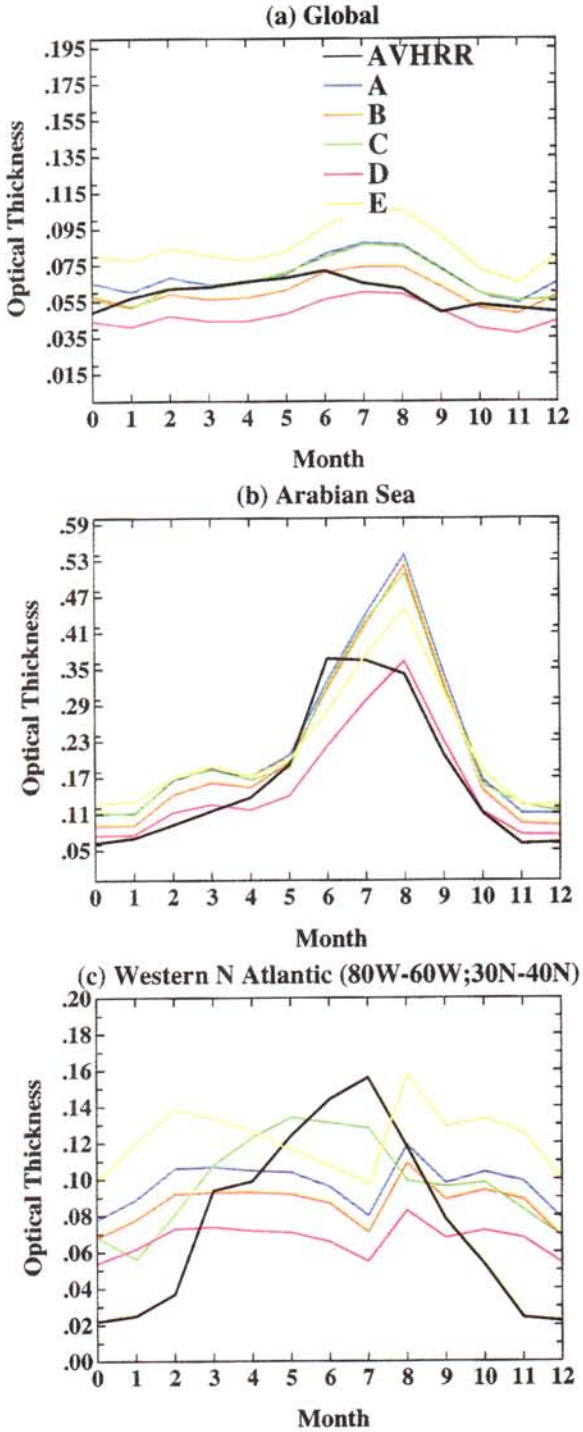

Plate 7. Comparison of the results from different model assumptions (solid lines) to the AVHRR optical thickness (dashed line). Case A is the "best estimate" case as in Plates 2–6. Case B is the biomass burning signal reduced by a factor of 2. Case C is the sulfate aerosol distribution of *Chuang et al.* [1997] instead of *Chin et al.* [1996]. Case D is the minimum assumption for specific extinction efficiencies B for all aerosol types (Table 1). Case E is the minimum extinction cross sections for absorbing aerosols (dust) and maximum values for the other aerosol types.

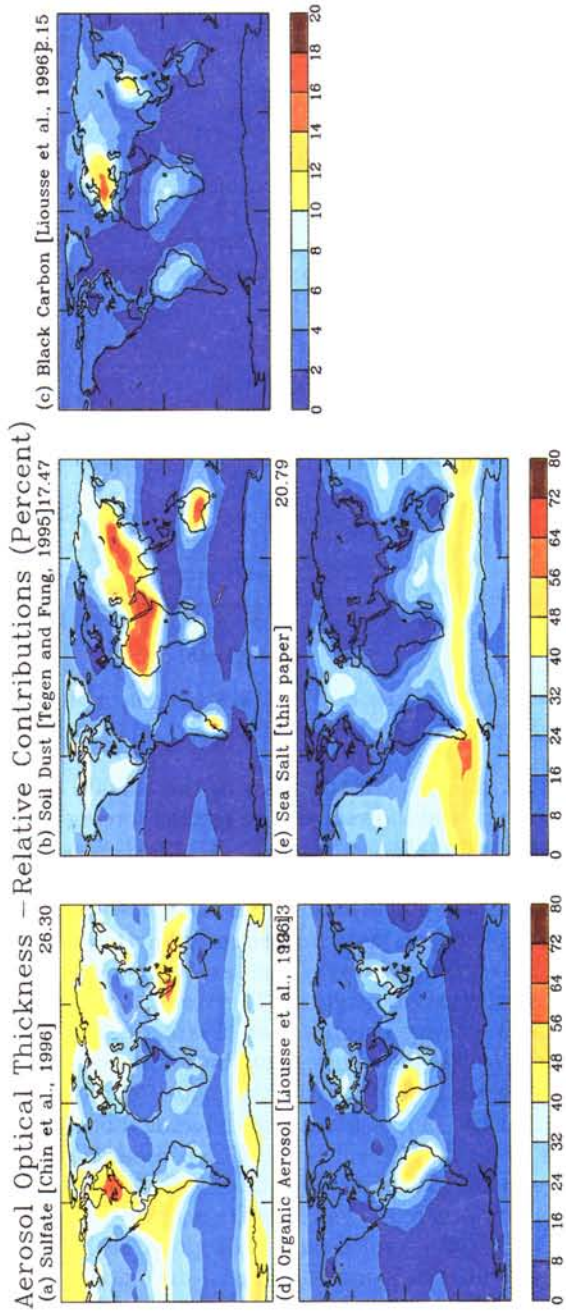

Plate 8. Annual mean relative contribution of the aerosol types sulfate, soil dust, organic and black carbon aerosol, and sea salt to the extinction optical thickness as estimated from transport model results. Note the different scale for the relative contribution of black carbon aerosol.

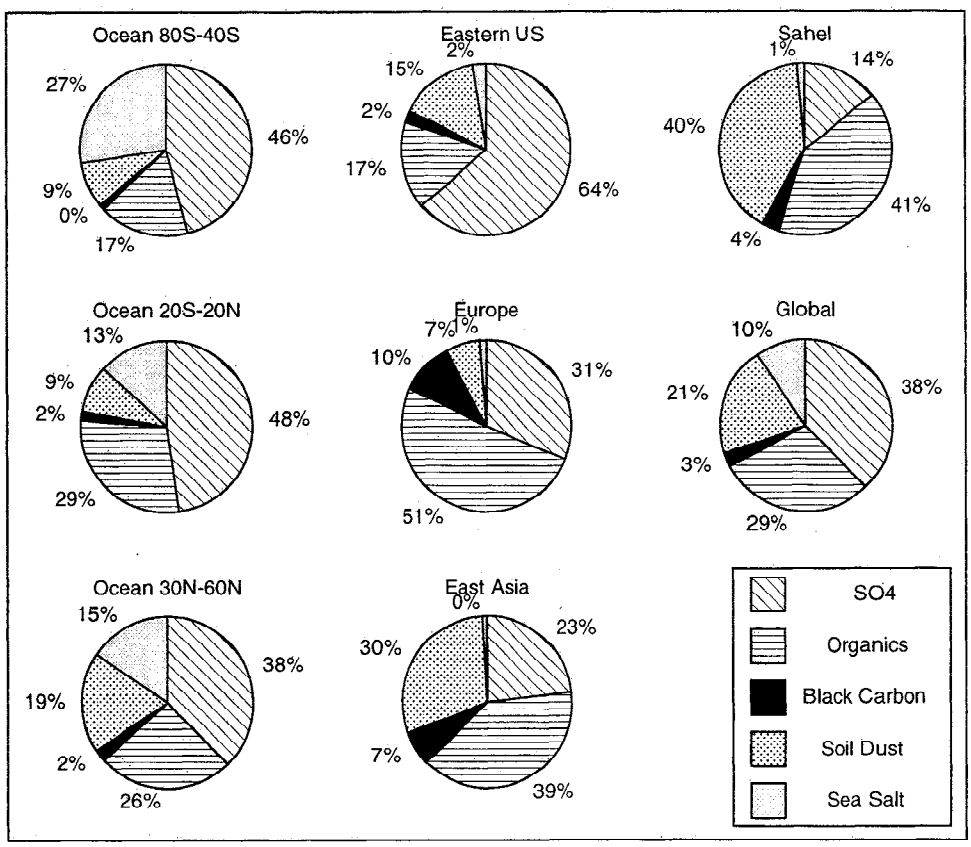

a

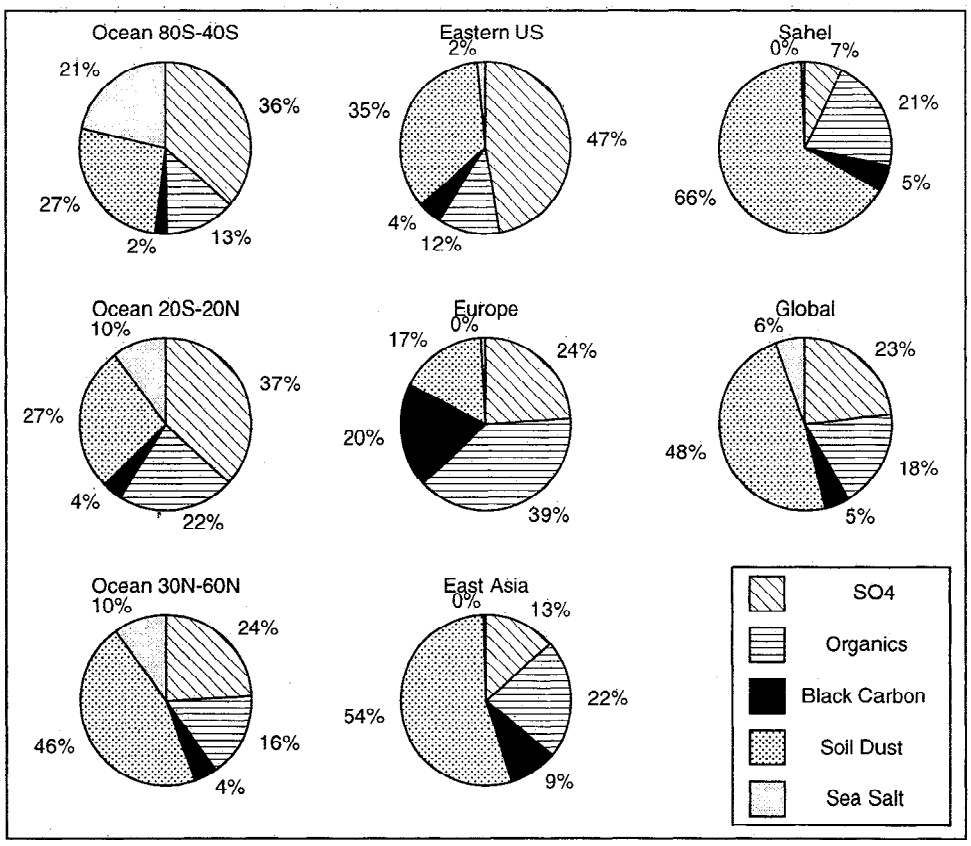

b

Figure 3. Aerosol "optical thickness" composition. (a) Minimum contribution of absorbing aerosol (specific extinction: clay, 1 m^2/g; silt, 0.2 m^2/g; SO_4 and organics, 8.5/14 m^2/g (land/ocean); black carbon, 8 m^2/g; and sea salt, 0.4 m^2/g). (b) Maximum contribution of absorbing aerosol (specific extinction: clay, 2 m^2/g; silt, 0.4 m^2/g; SO_4 and organics, 5/7 m^2/g (land/ocean); black carbon, 12m^2/g; and sea salt, 0.2 m^2/g).

1994]. The contribution of absorbing aerosol to the total aerosol load is also of interest, as this aerosol type (in contrast to nonabsorbing aerosol) increases atmospheric heating rates and could influence circulation patterns while not necessarily changing the radiation budget at the top of atmosphere. Therefore we attempt to estimate the range of the contribution of the main types of absorbing aerosols (dust and black carbon) to the total aerosol optical thickness for the model results. In Figures 3a and 3b compositions of the extinction optical thickness are given for the examples of three marine locations (80°S–40°S, 20°S–20°S, and 30°N–60°N) and four continental locations (eastern United States, western Europe, eastern Asia, and Sahel) and the global mean for the cases of maximum and minimum contribution of absorbing aerosols (soil dust and black carbon) to the total optical thickness. For the estimate of the range of the contribution

$$R_a = \frac{\tau_{\text{dust}} + \tau_{\text{black carbon}}}{\tau_{\text{all types}}}$$

of the absorbing aerosols, we compare optical thicknesses calculated from the maxima and minima of the extinction cross sections from the range given in Table 1. As the aerosol distributions resulting from the transport models contain uncertainties that are not taken into account in this estimate, the actual range in variations of the composition of aerosol optical thickness could be higher. The results for minimum and maximum dust and black carbon extinction compared with the maximum and minimum contribution of nonabsorbing aerosol (after subtracting the contribution of black carbon aerosol the carbonaceous aerosol was assumed to be nonabsorbing) lead to a wide range of possible compositions of aerosol optical thicknesses. In the global mean, absorbing aerosols contribute between 24% and 53% to the global aerosol optical thickness. The contribution of absorbing aerosols over the ocean regions varies between 9% and 46% in the latitudinal means (the maximum values occurring at latitudes with extensive biomass burning and dust source areas in the tropics and subtropics) and between 17% and 34% in the industrialized areas in the United States and Europe. The model results indicate that the black carbon contribution to the aerosol would be highest in Europe, with up to 20% of the total optical thickness possibly caused by this aerosol type. Recently, it has been found during the tropospheric aerosol radiative forcing observational experiment (TARFOX) that organics constitute about half of the aerosol load downwind the coast of NE United States while in the model the organic aerosol fraction is only about half of the sulfate fraction. This could mean that organics are underestimated in the model. The relative high modeled contribution of soil dust in this area is most likely an overestimate, caused by too-weak wet deposition in the dust model and too-strong wet deposition in the sulfate model. In areas close to large dust source regions like the Sahel and China, dust extinction dominates the aerosol optical thickness. The contribution of absorbing aerosol in those regions can vary between 37% and 71%. Over the oceans, sea-salt aerosol can contribute considerably to the aerosol optical thickness. It can contribute between 6% and 10% to the global mean and possibly up to 30% in the southern oceans (40°-80°S). Although this value is nonnegligible, sea salt can be treated as constant background aerosol because of its small spatial and temporal variability.

Plates 8a–8e summarize the annual mean composition of global aerosol optical thickness for the dominant species sulfate, soil dust, carbonaceous (organic + black carbon) aerosol, and sea salt, simulated by the transport models, expressed as percentage of total aerosol extinction optical thickness. For carbonaceous aerosol, the contributions of black carbon aerosol and (nonabsorbing) organic aerosol are shown separately. Sulfate dominates the aerosol extinction over the eastern United States, the southern oceans (in the southern hemisphere summer), and the tropical Pacific. The dominance of sulfates in the southern oceans can be explained by sulfate production from DMS emissions, which are highest during the southern hemisphere summer months. This signal cannot be distinguished in the northern hemisphere, because here the total aerosol load is higher. The high contribution of sulfate aerosol over the tropical Pacific can be explained by the fact that dust and carbonaceous aerosol loads are very low in that region because of the distance to the sources. Although the model results indicate that sulfate is the major contributor to aerosol extinction over the eastern United States, they also indicate that for the industrialized regions of Europe and China, carbonaceous aerosols are strong contributors, and in the case of Europe the black carbon contribution is very high. Other areas with strong contribution of carbonaceous aerosol are areas with high biomass burning emissions like Brazil and tropical Africa. Dust contribution is highest in the source areas in the Sahara, Arabia, Australia, and Asia. High dust contribution is found in areas with highest total optical thicknesses, emphasizing the importance of soil dust to the global aerosol extinction. Sea-salt contribution to the global aerosol optical thickness is generally low; only in the Southern Pacific can it contribute up to 40% due to the absence of other aerosol species.

5. Conclusions

Presently, uncertainties in the knowledge of global sources, transformation processes, and optical properties of aerosols result in a wide range of uncertainties in estimates of the optical thicknesses, and, consequently, the radiative effects of individual aerosol types. From results of several aerosol transport models that are based on current knowledge of aerosol processes and distributions and relatively crude estimates of their specific extinction cross sections, we estimate that globally, sulfate, soil dust, and carbonaceous aerosols contribute equally to the extinction aerosol optical thickness. There are, however, large regional and seasonal

differences in aerosol composition. The results show that any representation of global aerosol by a single aerosol type or by several types that are fixed in space and time (i.e., "urban," "rural," "remote," etc.) would be insufficient for studies of aerosol effects, specifically for studying the effects of changing aerosol levels for climate change scenarios. Instead, aerosol distributions and properties should be investigated for the main aerosol species individually so that a combined aerosol product can take into account variations in aerosol composition. The mixture of different aerosol types may lead to changes in aerosol properties. For example, a coating of soot or dust particles with sulfates would increase their hygroscopicity and aerosol particles could provide a surface for heterogeneous chemical reactions in the atmosphere, thereby influencing atmospheric chemistry [*Dentener et al.*, 1996]. By adsorbing sulfate aerosol particles (that could otherwise act as cloud condensation nuclei) on the surface of soil dust, those dust particles could actually cause a decrease of cloud droplet number compared with conditions of no coarse mode aerosol being present.

Aerosol distributions from either satellite retrievals, ground-based measurements, or transport models alone are not sufficient to describe a realistic global aerosol climatology that could be used to accurately calculate the radiative impact of aerosols and their influence on tropospheric chemistry. Ground-based measurements of aerosol optical thickness can potentially be used to constrain model results over land, although problems arise by comparing point measurements with multiyear mean model results averaged over a large area. For information on interannual variability of aerosol loads, such measurements should be continued for several years at the individual stations. Additional continuous measurements over east and Central Asia would be needed, as well as at remote stations in the southern oceans and in areas mainly influenced by desert dust in North Africa, to obtain a more complete global coverage of ground-based aerosol information. To account for the high spatial variability of aerosol load, it also would be useful to operate several instruments in an area covering several thousand square kilometers in specific regions of "typical" aerosol loads.

Comparisons of model results with satellite retrievals reveal both model inaccuracies and retrieval problems. With the current satellite instrumentation, preliminary information on aerosol composition (single scattering albedo) is needed for retrieval of aerosol optical thickness that can in turn be used to validate models. Here we find that the seasonal aerosol optical thickness signal from AVHRR is often well reproduced in the model composite, while the magnitude of the optical thickness is either overestimated or underestimated. For soil dust aerosol, the comparison of the model results with both AVHRR retrievals and Sun photometer measurements reveals that the model apparently underestimates dust emission in the Saharan-Sahelian region in the northern hemisphere summer, while in other regions influenced by soil dust the seasonal dust distribution is well reproduced; however, the AVHRR retrieval appears to underestimate the aerosol signal by assuming a completely scattering aerosol, while in reality, dust is partly absorbing solar radiation. For regions where the aerosol load is dominated by biomass burning aerosol, the comparison with Sun photometer data shows that the model underestimates the aerosol optical thickness during burning season, which may be caused by problems occurring with the comparison of point measurements and a large model grid box. Downwind of the South American biomass burning region, no smoke aerosol signal can be observed in the AVHRR retrievals, which may be caused by clouds obscuring the aerosol signal. On the other hand, this would indicate that the carbonaceous aerosol does not underestimate the aerosol sources on a larger scale, as one could suspect from the comparison with the Sun photometer data. In the North Atlantic, which is mainly influenced by industrial aerosol, the AVHRR signal is higher than the modeled aerosol optical thickness; this difference may be caused by an overestimate of wet deposition for the sulfate aerosol or by underestimating the emission of carbonaceous aerosol by industrial sources.

While many studies on global aerosol effects presently concentrate only on sulfate aerosol, the contribution of absorbing aerosol to the aerosol extinction is important for studies of climate effects and remote sensing applications. While pure scattering aerosol like sulfate leads to a decrease of incoming solar radiation at the ground (and therefore leads to surface cooling), the presence of absorbing aerosol can change the vertical temperature profile which could regionally influence atmospheric dynamics. The uncertainty in the contribution of absorbing as well as nonspherical aerosol also could lead to errors in satellite retrievals of aerosol optical thickness. To improve our knowledge of aerosol distribution, further ground-based and satellite measurements of aerosol distribution and optical properties are needed. As aerosol optical properties can vary widely, satellite retrievals should make use of spectrally resolved information as well as of changes in polarization degree caused by aerosols.

Acknowledgments. This work was supported by the NASA Earth Observing Systems (EOS) program; NASA grant NAG5-4052 (I.T.); NASA grant NAGI-1909 to Harvard University (D.J. and M.C.); the NASA Atmospheric Chemistry, Modeling, and Analysis Program (J.P.); the Swiss National grant 2100-037698.98 (P.H.), and the Climate System History and Dynamics Programme that is jointly sponsored by the Natural Sciences and Engineering Research Council of Canada and the Atmospheric Environment Service of Canada (I.F.). Sea-salt aerosol data were supplied by D. Savoie and J. Prospero, University of Miami. We thank two anonymous reviewers for helpful suggestions.

References

Ackerman, S. A., and S. K. Cox, Surface weather observations of atmospheric dust over the southest summer

monsoon region, *Meteorol. Atmos. Phys.*, *41*, 319–349, 1989.

Andreae, M. O., Climate effects of changing atmospheric aerosol levels, in *World Survey of Climatology*, vol. 16, *Future Climate of the World*, edited by A. Henderson-Sellers, Elsevier, New York, 1995.

Artaxo, P., F. Gerab, M. A. Yamasoe, and J. V. Martins, Fine mode aerosol composition at three long-term atmospheric monitoring sites in the Amazon basin, *J. Geophys. Res.*, *99*, 22,857–22,868, 1994.

Balkanski, Y. J., D. J. Jacob, G. M. Gardner, W. C. Graustein, and K. K. Turekian, Transport and residence times of tropospheric aerosols inferred from a global three-dimensional simulation of ^{210}Pb, *J. Geophys. Res.*, *98*, 20,573–20,586, 1993.

Bates, T. S., J. D. Cline, R. H. Gammon, and S. R. Kelly-Hansen, Regional and seasonal variations in the flux of oceanic dimethylsulfide to the atmosphere, *J. Geophys. Res.*, *92*, 2930–2938, 1987.

Benkovitz, C. M., T. Scholtz, J. Pacyna, L. Tarrason, J. Dignon, E. C. Voldner, P. A. Spiro, J. A. Logan, and T. E. Graedel, Global gridded inventories of anthropogenic emissions of sulfur and nitrogen, *J. Geophys. Res.*, *101*, 29,239–29,253, 1996.

Boucher, O., and U. Lohmann, The sulfate–CCN–cloud albedo effect: A sensitivity study with two general circulation models, *Tellus*, *47B*, 281–300, 1995.

Charlson, R. J., D. S. Covert, and T. V. Larson, Observation of the effect of humidity on light scattering by aerosols, in *Hygroscopic Aerosols*, edited by L. Ruhnke and A. Deepak, pp. 35–44, A. Deepak, Hampton, Va., 1984.

Chin, M., D. J. Jacob, G. M. Gardner, P. A. Spiro, M. Foreman-Fowler, and D. L. Savoie, A global three-dimensional model of tropospheric sulfate, *J. Geophys. Res.*, *101*, 18,667–18,690, 1996.

Chuang, C. C., J. E. Penner, K. E. Taylor, A. S. Grossmann, and J. J. Walton, An assessment of the radiative effects of anthropogenic sulfate-containing aerosols, *J. Geophys. Res.*, *102*, 3761–3778, 1997.

Cooke, W., B. Koffi, and J. M. Gregoire, Seasonality of vegetaion fires in Africa from remote sensing data and application to a global chemistry model, *J. Geophys. Res.*, *101*, 21,051–21,065, 1996.

d'Almeida, G., and L. Schütz, Number, mass, and volume distribution of mineral aerosol and soils of the Sahara, *J. Clim. Appl. Meteorol.*, *22*, 233–243, 1983.

Dentener, F. J., and P. J. Crutzen, Reaction of $N_2 2O_5$ on tropospheric aerosols: Impact on the global distributions of NO_x, O_3, and OH, *J. Geophys. Res.*, *98*, 7149–7163, 1993.

Dentener, F. J., G. R. Carmichael, Y. Zhang, J. Lelieveld, and P. J. Crutzen, Role of mineral aerosol as reactive surface in the global troposphere, *J. Geophys. Res.*, *101*, 22,869–22889, 1996.

Erickson, D. J., and R. A. Duce, On the global flux of atmospheric sea salt, *J. Geophys. Res.*, *93*, 14,079–14,088, 1988.

Erickson, D. J., J. T. Merrill, and R. A. Duce, Seasonal estimates of global atmospheric sea-salt distribution, *J. Geophys. Res.*, *91*, 1067–1072, 1986.

Fung, I., K. Prentice, E. Matthews, and G. Russell, Three-dimensional tracer model study of atmospheric CO_2: Response to seasonal exchanges with the terrestrial biosphere, *J. Geophys. Res.*, *88*, 1281–1294, 1983.

Gao, Y., R. Arimoto, J. T. Merril, and R. A. Duce, Relationships between the dust concentrations over eastern Asia and the remote North Pacific, *J. Geophys. Res.*, *97*, 9867–9872, 1992.

Genthon, C., Simulations of desert dust and sea salt aerosols in Antarctica with a general circulation model of the atmosphere, *Tellus*, *44B*, 371–389, 1992.

Gillette, D., A wind tunnel simulation of the erosion of soil: Effect of soil texture, sandblasting, wind speed, and soil consolidation on dust production, *Atmos. Environ.*, *12*, 1735–1743, 1978.

Gomes, L., G. Bergametti, G. Coudé-Gaussen, and P. Rognon, Submicron desert dusts: A sandblasting process, *J. Geophys. Res.*, *95*, 13,927–13,935, 1990.

Holben, B. N., A. Setzer, T. F. Eck, A. Pereira, and I. Slutsker, Effect of dry–season biomass burning on Amazon basin aerosol concentrations and optical properties, 1992–1994, *J. Geophys. Res.*, *101*, 19,465–19,481, 1996.

Intergovernmental Panel on Climate Change, Climate Change 1994, edited by Houghton et al., Cambridge Univ. Press, New York, 1994.

Kalma, J. D., J. G. Speight, and R. J. Wasson, Potential wind erosion in Australia: A continental perspective, *J. Clim.*, *8*, 411–428, 1988.

Kiehl, J. T., and B. P. Briegleb, The relative importance of sulfate aerosols and greenhouse gases in climate forcing, *Science*, *260*, 311–314, 1993.

Kiehl, J. T., and H. Rodhe, Modeling geographical and seasonal forcing due to aerosols, in *Aerosol Forcing of Climate*, edited by R. Charlson and J. Heintzenberg, pp. 281–296, John Wiley, New York, 1995.

Lacis, A. A., and M. I. Mishchenko, Climate forcing, climate sensitivity, and climate response: A radiative modeling perspective on atmospheric aerosols, in *Aerosol Forcing of Climate*, edited by R. Charlson and J. Heintzenberg, 11–42, John Wiley, New York, 1995.

Langner, J., and H. Rodhe, A global three-dimensional model of the tropospheric sulfur cycle, *J. Atmos. Chem.*, *13*, 225–263, 1991.

Li, X., H. Maring, D. Savoie, K. Voss, and J. M. Prospero, Dominance of mineral dust in aerosol light-scattering in the North Atlantic trade winds, *Nature*, *380*, 416–419, 1996.

Liousse, C., J. E. Penner, C. Chuang, J. J. Walton, H. Eddleman, and H. Cachier, A global three-dimensional model study of carbonaceous aerosols, *J. Geophys. Res.*, *101*, 1996, 19,411–19,432.

Meszaros, A., and K. Vissy, Concentration, size distribution, and chemical nature of atmospheric aerosol particles in remote oceanic areas, *J. Aerosol Sci.*, *5*, 101–109, 1974.

Middelton, N., *World Atlas of Desertification*. Edward Arnold, London, 1992.

Mishchenko, M. I., and L. D. Travis, Light scattering by polydispersions of randomly oriented spheroids with sizes comparable to wavelengths of observation, *Appl. Opt.*, *33*, 7206–7225, 1994.

Oceanography Course Team, *Seawater: It's Composition, Properties and Behaviour.* Pergamon Press, Tarrytown, N.Y., 1989.

Patterson, E., and D. Gillette, Commonalities in measured size distributions for aerosols having a soil-derived component, *J. Geophys. Res.*, *82*, 2074–2082, 1977.

Pham, M., J. F. Muller, G. Brasseur, C. Granier, and G. Megie, A three-dimensional study of the tropospheric sulfur cycle, *J. Geophys. Res.*, *100*, 26,061–26,092, 1995.

Prather, M. J., B. McElroy, S. C. Wofsy, G. R. Russell, and D. Rind, Chemistry of the global troposphere: Fluorocarbons as tracers of air motion, *J. Geophys. Res.*, *92*, 6579–6613, 1987.

Prospero, J. M., and R. T. Nees, Impact of the North African drought and El Niño on mineral dust in the Barbados trade winds, *Nature*, *320*, 735–738, 1986.

Rao, C. R. N., L. L. Stowe, E. P. McClain, J. Sapper, and M. P. McCormick, Development and application of aerosol remote sensing with AVHRR data from the NOAA satellites, in *Aerosols and Climate*, edited by P. V. Hobbs, A. Deepak, Hampton, Va., 1988.

Reynolds, M. R., and D. C. Marisco, An improved real-time global sea-surface temperature analysis, *J. Clim.*, *6*, 114–119, 1993.

Shea, D., Climatological atlas: 1950–1979, surface air temperature, precipitation, sea level pressure, and sea surface temperature, Technical Report NCAR/TN-269+STR, Natl. Cent. for Atmos. Res., Boulder, Co., 1986.

Spivakovsky, C. M., M. R. Revich, J. A. Logan, S. C. Wofsy, M. B. McElroy, and M. J. Prather, Tropospheric OH in a three-dimensional chemical tracer model: An assessment based on observations of CH_3CCL_3, *J. Geophys. Res.*, *95*, 18,441–18,472, 1990.

Tegen, I., and I. Fung, Modeling of mineral dust in the atmosphere: Sources, transport, and optical thickness, *J. Geophys. Res.*, *99*, 22,897–22,914, 1994.

Tegen, I., and I. Fung, Contribution to the mineral aerosol load from land surface modification, *J. Geophys. Res.*, *100*, 18,707–18,726, 1995.

Tegen, I., and A. A. Lacis, Modeling of particle size distribution and its influence on the radiative properties of mineral dust aerosol, *J. Geophys. Res.*, *101*, 19,237–19,244, 1996.

Tegen, I., A. Lacis, and I. Fung, The influence of mineral aerosol from disturbed soils on the global radiation budget, *Nature*, *380*, 419–422, 1996.

Tucker, C. J., H. E. Dregne, and W. W. Newcomb, Expansion and contraction of the Sahara desert from 1980 to 1990, *Science*, *253*, 299–301, 1991.

Walton, J. J., M. C. MacCracken, and S. J. Gahn, A global-scale Lagrangian trace species model of transport, transformation, and removal processes, *J. Geophys. Res.*, *93*, 8339–8345, 1988.

Webb, R., C. Rosenzweig, and E. R. Levine, A global data set of particle size properties, *NASA Tech. Rep. TM-4286*, 33 pp., 1991.

Wesley, M. L., and B. B. Hicks, Some factors that affect the deposition rates of sulfur dioxide and similar gases on vegetation, *J. Air. Pollut. Control Assoc.*, *27*, 1110–1116, 1977.

World Resources Institute, *World Resources 1992–1993*, edited by A. L. Hammond. Oxford Univ. Press, New York, 1992.

Zobler, L., A world soil file for global climate modeling, *NASA Tech. Rep. TM-87802*, 32 pp., 1986.

M. Chin, NASA Goddard Space Flight Center, Code 916, Greenbelt, MD 20771 (e-mail: chin@gsfc.nasa.gov)

I. Fung, School of Earth and Ocean Sciences, University of Victoria, P.O. Box 1700, Victoria, British Columbia, V8W 2Y2, Canada, (e-mail: inez@garryoak.seaoar.uvic.ca)

P. Hollrigl, Department of Geography, Division of Climate Research, Swiss Federal Institute of Technology, Zurich, Switzerland (e-mail: holli@geo.umnw.ethz.ch)

D. Jacob, Division of Engineering and Applied Science, Harvard University, Cambridge, MA 02138 (e-mail: djj@harvard.edu)

J. Penner, Dept. of Atmospheric, Oceanic, and Space Sciences, University of Michigan (e-mail: penner@umich.edu)

I. Tegen, Department of Applied Physics, Columbia University, and NASA Goddard Institute for Space Studies, 2880 Broadway, New York, NY 10025. (e-mail: itegen@giss.nasa.gov)

(Received March 11, 1997; revised June 19, 1997; accepted June 19, 1997.)